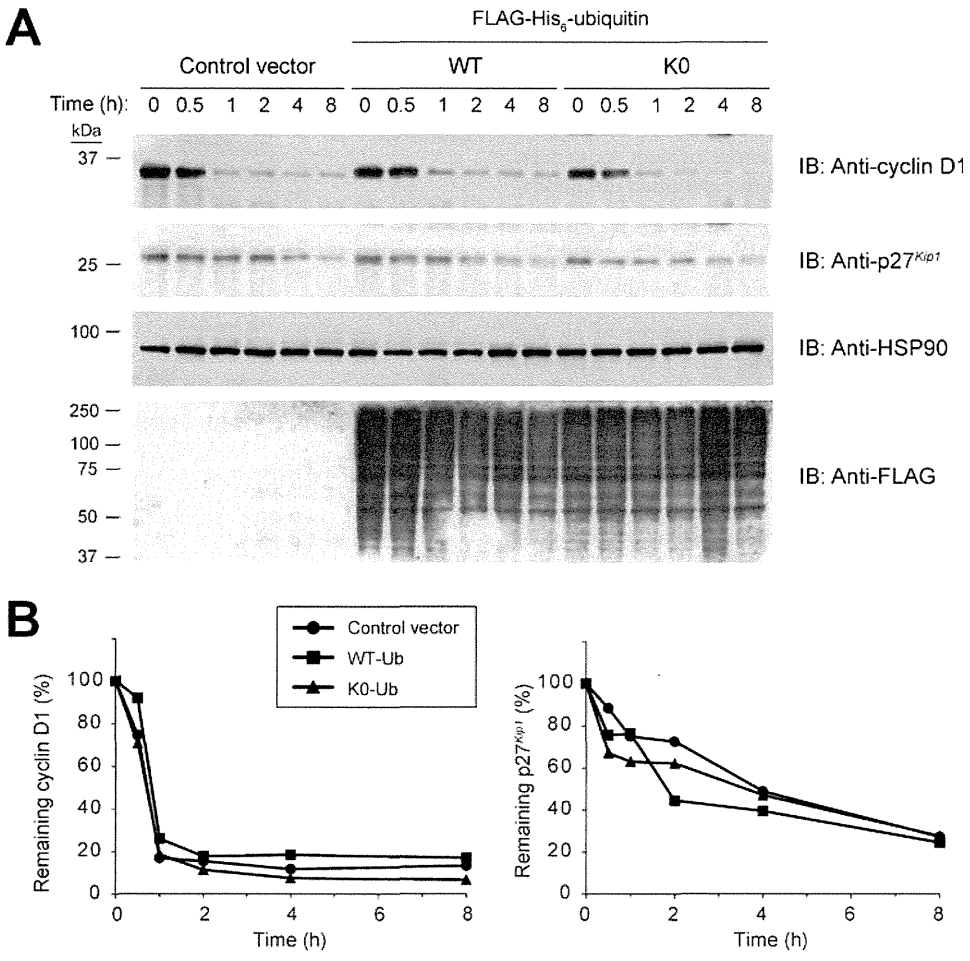

Figure 3. Effect of K0-Ub expression on the degradation of known ubiquitin—proteasome substrates. (A) The stability of endogenous cyclin D1 and $p27^{Kip1}$ in HEK293T cells expressing FLAG-His_6-tagged forms of WT-Ub or K0-Ub was monitored by incubation of the cells with CHX for the indicated times followed by immunoblot analysis with anti-cyclin D1 and anti-$p27^{Kip1}$. The blot was also probed with anti-HSP90 as a loading control and with anti-FLAG to reveal overall ubiquitylation. (B) The abundance of cyclin D1 or $p27^{Kip1}$ in the experiment shown in (A) was determined by densitometry, normalized by that of HSP90, and expressed relative to the value for time zero.

and each reaction mixture was subjected to SDS-PAGE on a 12% gel followed by blot analysis with a horseradish peroxidase (HRP)-streptavidin conjugate (SouthernBiotech, Birmingham, AL). To preserve thioester bonds in E1 and E2, we terminated the reaction under nonreducing conditions by using SDS sample buffer without 2-mercaptoethanol (2-ME).

In Vitro Assay of $p27^{Kip1}$ Ubiquitylation

Human $p27^{Kip1}$ cDNA was subcloned into pGEX-6P for production of the GST-tagged protein in bacteria. The K165R mutant of $p27^{Kip1}$ was constructed by replacing the codon for Lys^{165} with a codon for arginine by site-directed mutagenesis with the use of a QuickChange kit (Stratagene, La Jolla, CA). GST-tagged $p27^{Kip1}$ (WT or K165R) proteins were expressed in *E. coli* strain BL21 (DE3) pLys(S) cultured in the presence of 500 μM IPTG. The bacterial cells were resuspended in 50 mM Tris-HCl (pH 7.5) containing 500 mM NaCl and then lysed by ultrasonic treatment. The lysate was centrifuged at 20 000*g* for 10 min at 4 °C to remove debris, and the resulting supernatant was mixed with glutathione—Sepharose 4B with rotation at 4 °C for 30 min. The beads were then washed with 50 mM Tris-HCl (pH 7.5) containing 500 mM NaCl, and the GST-tagged proteins were eluted with 50 mM Tris-HCl (pH 7.5) containing 10 mM reduced glutathione. The purity of the recombinant proteins was confirmed by SDS-PAGE and staining with Coomassie brilliant blue G-250 (data not shown).

For in vitro assay of $p27^{Kip1}$ ubiquitylation, we prepared a ubiquitin ligase fraction from HEK293T cells. The cells were washed with phosphate-buffered saline, suspended in hypotonic buffer containing 20 mM Tris-HCl (pH 7.5), 10 mM KCl, 1.5 mM $MgCl_2$, and 250 mM sucrose, and subjected to three cycles of freezing and thawing. The resulting lysate was centrifuged at 100000*g* for 4 h at 4 °C, and the resulting supernatant (S100Pr−), from which proteasomes had been removed, was retrieved and frozen at −80 °C.

One microgram of GST-tagged $p27^{Kip1}$ (WT or K165R) was incubated for various times at 30 °C in a final volume of 20 μL with S100Pr− (8 μg), hemagglutinin epitope (HA)-tagged ubiquitin (0.5 μg),[28] Ub-CHO (100 μg/mL), 1 mM dithiothreitol, a protease inhibitor mixture (aprotinin, leupeptin, and PMSF each at 10 μg/mL), and a proteasome inhibitor (10 μM MG132) in the presence of an ATP-regenerating system [25 mM Tris-HCl (pH 7.5), 120 mM NaCl, 1 mM $MgCl_2$, 2 mM ATP, 1 mM creatine phosphate, phosphocreatine kinase (0.5 U/mL)].

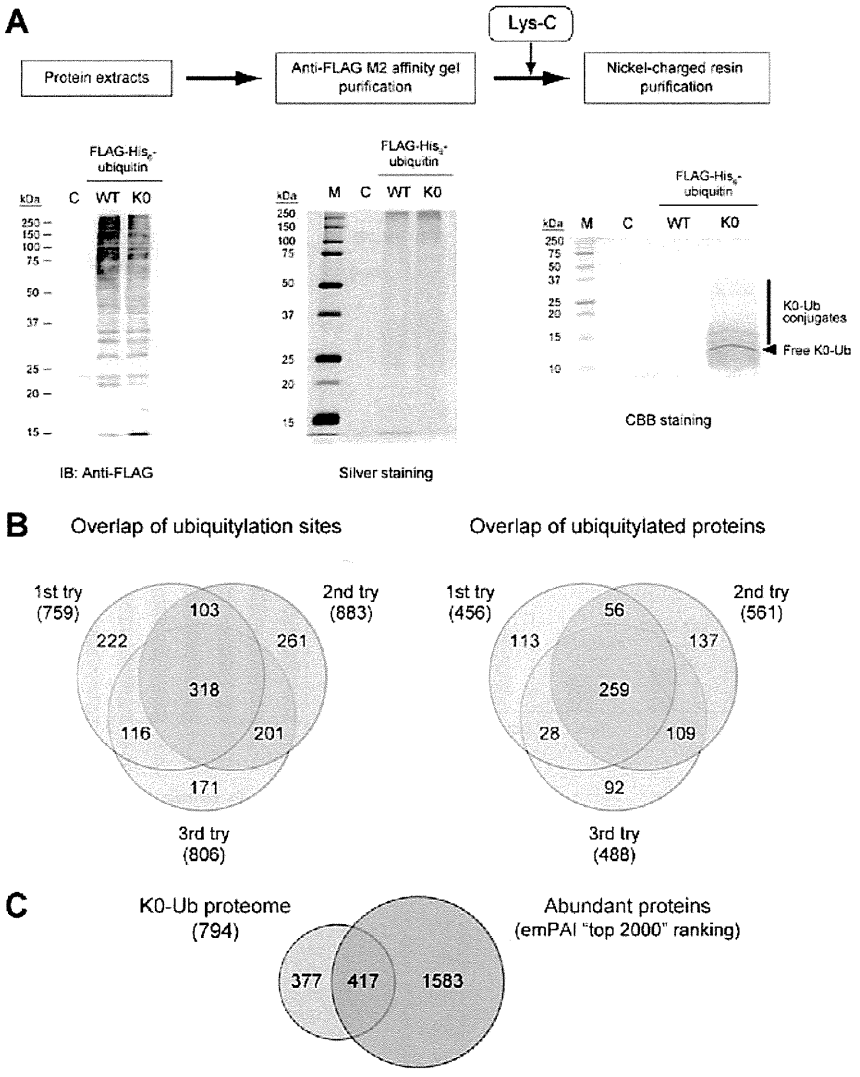

Figure 4. Overview of K0-Ub proteome analysis. (A) Protein extracts of HEK293T cells expressing FLAG-His_6-tagged WT-Ub or K0-Ub, or of cells transfected with the corresponding empty vector (C), were subjected to immunoblot analysis with anti-FLAG (left panel). The protein samples were subjected to purification with anti-FLAG M2 affinity gel and then analyzed by SDS-PAGE and silver staining (center panel; lane M, molecular size standards). After Lys-C treatment, which results in the digestion of WT-Ub conjugates but not that of K0-Ub conjugates, the protein samples were subjected to purification with nickel-charged resin followed by SDS-PAGE and staining with Coomassie brilliant blue G-250 (CBB) (right panel). (B) Venn diagrams showing overlap of K0-ubiquitylated sites and proteins in three independent experiments performed with HEK293T cells. (C) Venn diagram showing overlap of the K0-Ub proteome and abundant proteins (emPAI "top 2000" ranking) for HEK293T cells.

The reaction was terminated by the addition of SDS sample buffer, and each reaction mixture was subjected to SDS-PAGE on a 9% gel followed by immunoblot analysis with anti-GST.

In Vivo Assay of $p27^{Kip1}$ Ubiquitylation

HeLa cells were synchronized at the G_1−S transition with a double thymidine block. Between the first (2 mM thymidine for 18 h) and second (2 mM thymidine for 16 h) blocks, the cells were transfected with pcDNA3 vectors for His_6-tagged ubiquitin and HA-$p27^{Kip1}$ (WT or K165R). Proteins conjugated with His_6-tagged ubiquitin were purified from the transfected cells with nickel-charged resin under denaturing conditions, fractionated by SDS-PAGE, and subjected to immunoblot analysis with anti-HA.

Protein Degradation Analysis

HEK293T cells were transfected with pcDNA3 vectors for FLAG-His_6-tagged ubiquitin (WT-Ub or K0-Ub). For half-life studies, CHX (50 μg/mL) was added to the culture medium 24 h after transfection. At various times thereafter, the cells were lysed for measurement of endogenous protein abundance by immunoblot analysis.

Alternatively, HA-tagged human $p27^{Kip1}$ (WT or K165R) cDNA was subcloned into pcDNA3 for transfection of HEK293T cells. For half-life studies, CHX (50 μg/mL) was added to the medium 24 h after transfection. At various times thereafter, the cells were lysed and the abundance of HA-$p27^{Kip1}$ was measured by immunoblot analysis with anti-HA.

RESULTS AND DISCUSSION

Strategy for Identification of Ubiquitylation Sites

For comprehensive analysis of human ubiquitylated proteins, we have developed a new method for identification of ubiquitylation sites with the use of K0-Ub, in which all seven lysines of WT-Ub are replaced with arginine (Figure 1A). This method consists

dx.doi.org/10.1021/pr200668y | J. Proteome Res. 2012, 11, 796–807

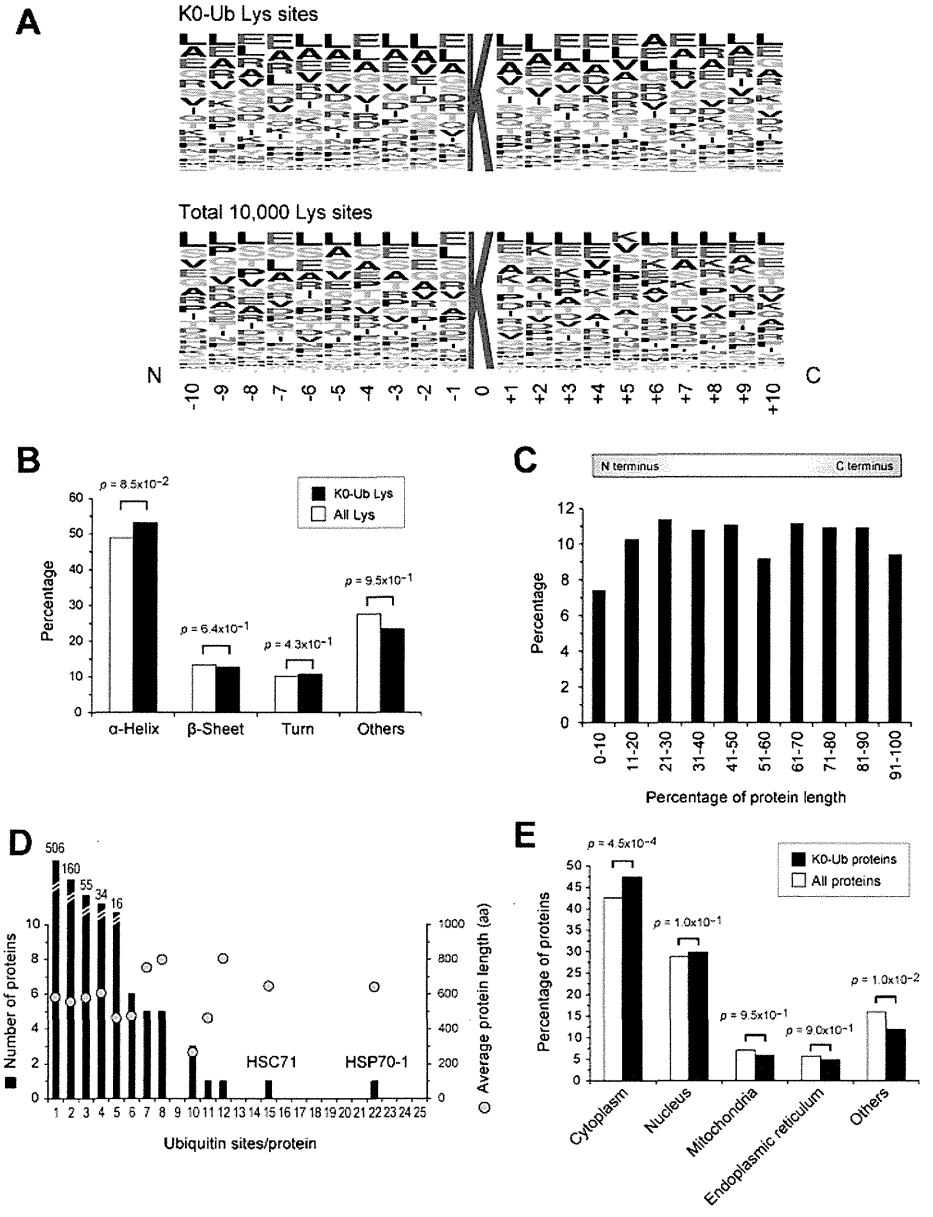

Figure 5. Properties of K0-ubiquitylated sites and proteins. (A) Sequence logo plots representing amino acid frequencies for ±10 amino acids relative to identified lysine ubiquitylation sites (upper panel). The sequence logo for 10 000 lysine residues randomly assigned from human IPI database version 3.16 is shown as a control (lower panel). (B) Distribution of secondary structures for all lysines and K0-ubiquitylated lysines obtained from an analysis of 151 PDB structures (290 K0-ubiquitylated lysines and 2463 total lysines). (C) Distribution of the 1392 identified ubiquitylation sites within their protein sequences. The length of each protein is normalized to 100%. (D) Number of ubiquitylation sites for the 794 identified ubiquitylated proteins. Average protein length in amino acids (aa) for proteins with the same number of ubiquitylation sites is indicated by circles. (E) Subcellular localization of all proteins and K0-ubiquitylated proteins determined by GO cellular component analysis.

of five steps: (i) affinity capture of proteins conjugated with FLAG- and His_6-tagged K0-Ub with anti-FLAG M2 affinity gel, (ii) digestion of the captured proteins with Lys-C, (iii) enrichment of peptides conjugated with K0-Ub with the use of nickel-charged resin, (iv) digestion of the peptides with trypsin, and (v) identification of ubiquitin signature peptides with nano-LC-MS/MS technology (Figure 1B). Given that neither K0-Ub nor the His_6 tags contain lysine residues and they are therefore resistant to digestion by Lys-C, peptides conjugated with His_6-K0-Ub are enriched by chromatography with nickel-charged resin. In contrast, peptides conjugated with His_6-WT-Ub are not recovered because WT-Ub undergoes multiple cleavages by Lys-C. The ubiquitin signature peptides are generated by in-gel tryptic digestion and identified by nanoLC-MS/MS.

Effect of K0-Ub Expression on Cellular Ubiquitylation

Excessive expression of K0-Ub might be expected to inhibit elongation of polyubiquitin chains and protein turnover, potentially affecting a variety of cellular functions. We thus examined the level of K0-Ub expression in HEK293T cells transiently transfected with a vector for FLAG-His_6-tagged K0-Ub. Cell lysates were fractionated by SDS−PAGE and subjected to immunoblot analysis with anti-FLAG. The extent of polyubiquitin chain elongation did not appear to differ between cells expressing WT-Ub and

Table 1. Identification by K0-Ub Proteome Analysis of Ubiquitylation Sites in Endogenous Ubiquitin

protein name (IPI accession number)	position	identified peptide sequence
UBIQUITIN (IPI00179330.6)	M1, K6:	M[a]QIFVK[a]TLTGKTITLEVEPSDTIENVK
	K6:	MQIFVK[a]TLTGK
	K6, K11:	MQIFVK[a]TLTGK[a]TITLEVEPSDTIENVK
	K11:	TLTGK[a]TITLEVEPSDTIENVK
	K11, K27:	TLTGK[a]TITLEVEPSDTIENVK[a]AK
	K27:	TITLEVEPSDTIENVK[a]AK
	K27, K29:	TITLEVEPSDTIENVK[a]AK[a]IQDK
	K33:	IQDK[a]EGIPPDQQR
	K48:	LIFAGK[a]QLEDGR
	K63:	TLSDYNIQK[a]ESTLHLVLR

[a] Ubiquitin signature site.

those expressing K0-Ub (Figure 2A), suggesting that forced expression of K0-Ub did not substantially perturb cellular ubiquitylation.

We next estimated the ubiquitylation rate for K0-Ub in vitro. We produced biotinylated ubiquitin for an in vitro ubiquitylation assay (Figure 2B). Biotinylated ubiquitin (WT-Ub or K0-Ub) was then incubated with E1, E2 (UbcH5c), and an ATP-regenerating system, and the rates of E1 and E2 conjugation to biotinylated ubiquitin were measured. The conjugation of K0-Ub to E1 or E2, which was reversed in the presence of 2-ME, appeared almost identical to that of WT-Ub (Figure 2C). Together, these results suggested that K0-Ub is suitable for in vitro ubiquitylation and is efficiently attached to cellular target proteins in vivo.

To evaluate further the effect of K0-Ub expression on ubiquitin-dependent protein degradation, we investigated the degradation rates of two representative proteins, cyclin D1 and $p27^{Kip1}$, that are targeted by the ubiquitin–proteasome system. Cyclin D1 is a short-lived protein, with a half-life of <1 h. CHX chase experiments revealed that expression of K0-Ub did not affect the rate of cyclin D1 degradation (Figure 3). Likewise, overexpression of K0-Ub did not result in a delay in $p27^{Kip1}$ degradation (Figure 3). Although we were unable to detect the ubiquitylation of endogenous p27 probably due to its low abundance, these results suggested that the expression of K0-Ub in our system affects neither cellular ubiquitylation nor subsequent protein degradation by the ubiquitin–proteasome system, consistent with the results of a recent report by Ziv et al.[29]

Comprehensive Identification of Protein Ubiquitylation Sites

With our new method, we next performed a comprehensive analysis to identify ubiquitylation sites of a large number of proteins in human cells. HEK293T cells were transfected with a vector encoding FLAG-His_6-tagged WT-Ub (control) or K0-Ub, and cell lysates were subjected to immunoblot analysis with anti-FLAG, revealing that the expression levels of WT-Ub and K0-Ub were similar (Figure 4A). The lysates were then subjected to purification with anti-FLAG M2 affinity gel followed by Lys-C digestion and purification with nickel-charged resin, and the resulting samples were fractionated by SDS-PAGE and stained with Coomassie brilliant blue G-250 (Figure 4A). The samples derived from cells expressing K0-Ub contained K0-Ub conjugates that migrated more slowly than did free K0-Ub, whereas no signal was visible with the samples derived from cells expressing WT-Ub. The purified peptides were further digested with trypsin and subjected to LC–MS/MS analysis.

We identified >750 ubiquitylation sites in a single analysis of HEK293T cells (Figure 4B). Three independent analyses resulted in the identification of 1392 ubiquitylation sites of 794 proteins, with the overall false discovery rate for peptides and proteins being <1% (Supplementary Tables S1 and S2, Supporting Information). The false discovery rate for ubiquitylated lysine–containing peptides, as opposed to all peptides, was even lower (0.3–0.4%).

We compared the identified ubiquitylated proteins with the abundant proteins of HEK293T cells ranked by the exponentially modified protein abundance index (emPAI "top 2000" ranking), which is calculated from the number of observed peptides per protein and the number of observable peptides per protein (Supplementary Table S3, Supporting Information). About half of the ubiquitylated proteins were not included among the "top 2000" abundant proteins (Figure 4C), suggesting that not only highly abundant proteins but also proteins of low abundance can be detected by our method. These results further suggest that the ubiquitinylated proteome differs from the total proteome.

Bioinformatics Analysis of Ubiquitylated Sites and Proteins

To gain insight into how lysine ubiquitylation might be regulated at the level of primary structure, we analyzed our data for local sequence context by extracting a ±10-residue sequence window surrounding each ubiquitylation site (Figure 5A). We compared the sequence logo for the identified ubiquitylation sites to that for 10 000 randomly assigned lysine residues (Figure 5A). Overall, no significant sequence recognition motif was detected among the identified ubiquitylation sites, possibly because they reflect reactions catalyzed by numerous E3 ligases.[30] We next compared the secondary structures around ubiquitylated lysines to those around all lysines. Structural information was available in the Protein Data Bank (PDB) for 151 of the 794 ubiquitylated proteins identified in our study, with these 151 proteins containing 290 ubiquitylated lysines and 2463 lysines in total. There was no statistically significant difference between ubiquitylated lysines and all lysines in secondary structure groups (Figure 5B), suggesting that ubiquitylation does not show any preference for primary or secondary structures. We also examined the position and number of ubiquitylation sites within identified proteins. The ubiquitylation sites were found to be evenly distributed throughout the identified proteins, with no significant bias toward the NH_2- or COOH-terminus (Figure 5C).

dx.doi.org/10.1021/pr200668y |J. Proteome Res. 2012, 11, 796–807

Table 2. Identification by K0-Ub Proteome Analysis of Ubiquitylation Sites of Proteins Related to Cell Cycle and DNA Damage and Repair

IPI accession number	protein name	position	identified peptide sequence
	Cell Cycle Related		
IPI00026689.4	CELL DIVISION CONTROL PROTEIN 2 HOMOLOGUE	K58:	EISLLK[a]ELR
		K136:	DLKPQNLLIDDK[a]GTIK
		K207:	K[a]PLFHGDSEIDQLFR
IPI00007811.1	CELL DIVISION PROTEIN KINASE 4	K211:	RK[a]PLFCGNSEADQLGK
IPI00023529.1	CELL DIVISION PROTEIN KINASE 6	K26:	ADQQYECVAEIGEGAYGK[a]VFK
IPI00025087.1	CELLULAR TUMOR ANTIGEN P53	K120:	LGFLHSGTAK[a]SVTCTYSPALNK
		K321:	KK[a]PLDGEYFTLQIR
		K357:	DAQAGK[a]EPGGSR
		K370:	AHSSHLK[a]SK
IPI00006991.1	CYCLIN-DEPENDENT KINASE INHIBITOR 1B ($p27^{Kip1}$)	K165:	RPATDDSSTQNK[a]R
IPI00184330.5	DNA REPLICATION LICENSING FACTOR MCM2	K591:	GVCLIDEFDK[a]MNDQDR
IPI00013214.1	DNA REPLICATION LICENSING FACTOR MCM3	K351:	GDINILLIGDPSVAK[a]SQLLR
		K435:	VTIAK[a]AGIHAR
IPI00018349.5	DNA REPLICATION LICENSING FACTOR MCM4	K536:	GQYTSGK[a]GSSAVGLTAYVMK
		K600:	SVLHEVMEQQTLSIAK[a]AGIICQLNAR
		K628:	K[a]TTIENIQLPHTLLSR
IPI00031517.1	DNA REPLICATION LICENSING FACTOR MCM6	K313:	FGGK[a]ELRDEEQTAESIK
		K422:	AVYTSGK[a]ASSAAGLTAAVVR
		K517:	SLK[a]QNINLSAPIMSR
		K611:	DGSGVTK[a]SSWR
IPI00299904.3	DNA REPLICATION LICENSING FACTOR MCM7	K145:	FELYFQGPSSNK[a]PR
		K387:	GNINICLMGDPGVAK[a]SQLLSYIDR
		K471:	TAIHEVMEQQTISIAK[a]AGILTTLNAR
		K648:	DSLLGDK[a]GQTAR
IPI00026309.3	GEMININ	K139:	ENK[a]ELAEVAEHVQYMAELIER
	DNA Damage and Repair		
IPI00412298.3	ATAXIA TELANGIECTASIA AND RAD3-RELATED PROTEIN	K1057:	ALHYLK[a]NETEIELGSLLR
IPI00178431.11	ATP-DEPENDENT DNA HELICASE Q1	K38:	QQELIQK[a]K
IPI00075081.1	FANCONI ANEMIA GROUP D2 PROTEIN	K561:	K[a]QLSSTVFK
IPI00024579.1	POSTREPLICATION REPAIR PROTEIN RAD18	K186:	SVEEIAPDPSEAK[a]RPEPPSTSTLK
		K197:	RPEPPSTSTLK[a]QVTK
		K309:	SAAEIVQEIENIEK[a]TR
		K462:	DLLEEEEAWEASHK[a]NDLQDTEISPR
		K218:	VDCPVCGVNIPESHINK[a]HLDSCLSR
IPI00021700.3	PROLIFERATING CELL NUCLEAR ANTIGEN	K80:	ILK[a]CAGNEDIITLR
		K164:	DLSHIGDAVVISCAK[a]DGVK
		K254:	YYLAPK[a]IEDEEGS
IPI00291939.1	STRUCTURAL MAINTENANCE OF CHROMOSOME 1	K1196:	EEFYTK[a]AESLIGVYPEQGDCVISK
IPI00008219.1	UV EXCISION REPAIR PROTEIN RAD23 HOMOLOGUE A	K47:	DAFPVAGQK[a]LIYAGK
		K53:	LIYAGK[a]ILSDDVPIR
		K78:	NFVVVMVTK[a]TK
		K122:	EDK[a]SPSEESAPTTSPESVSGSVPSSGSSGR
IPI00102997.1	WERNER HELICASE-INTERACTING PROTEIN 1	K457:	VLITENDVK[a]EGLQR

[a] Ubiquitin signature site.

Our analysis indicated that 506 out of the 794 identified proteins contained only a single lysine conjugated with ubiquitin, whereas the remaining 288 proteins contained multiple lysines that underwent ubiquitylation (Figure 5D). HSP70-1 and HSC71 were found to be ubiquitylated on at least 22 and 15 lysines, respectively, although the biological relevance of such extensive ubiquitylation of a chaperone molecule remains unknown. In addition, there was no apparent correlation between the number of ubiquitylation sites and protein length (Figure 5D). We next analyzed the subcellular localization of identified proteins on the basis of the "cellular component" of Gene Ontology (GO) slim annotations. The frequency of cytoplasmic localization for ubiquitylated proteins was slightly greater than that for total proteins (Figure 5E).

dx.doi.org/10.1021/pr200668y |J. Proteome Res. 2012, 11, 796–807

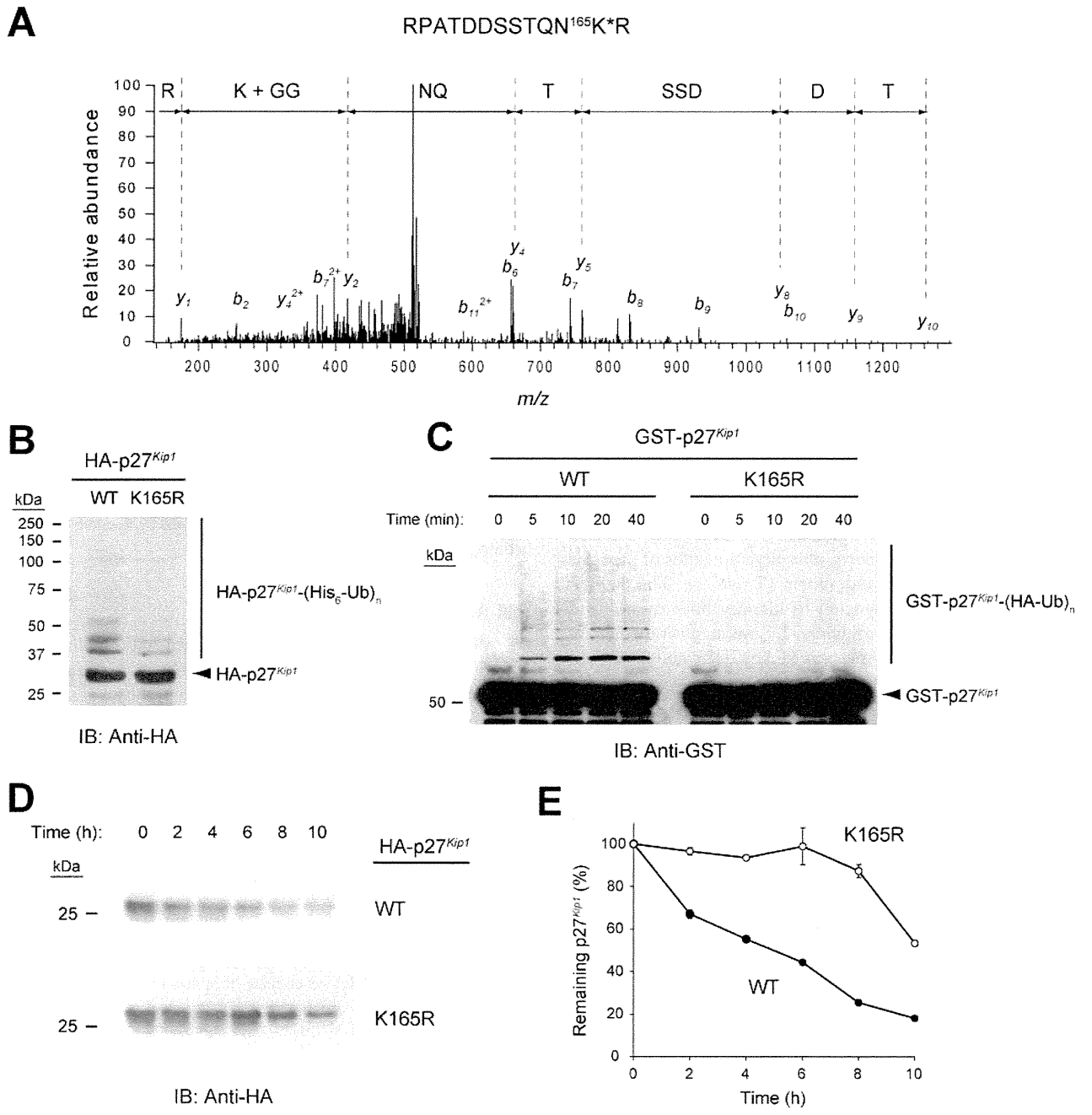

Figure 6. Lysine at position 165 is essential for ubiquitylation and degradation of $p27^{Kip1}$. (A) Our method identified Lys^{165} of $p27^{Kip1}$ as a ubiquitylation site. The diglycine-modified lysine was detected by MS/MS analysis with CID fragmentation. (B) HeLa cells were synchronized at the G_1−S boundary of the cell cycle by double thymidine block. After the first block, the cells were transfected with vectors for His_6-tagged ubiquitin (His_6-Ub) and either wild-type or K165R mutant forms of HA-tagged $p27^{Kip1}$. After the second block, proteins conjugated with His_6-Ub were purified under denaturing conditions and subjected to immunoblot analysis with anti-HA. The arrowhead indicates the position of unmodified HA-$p27^{Kip1}$. (C) Recombinant GST-tagged wild-type or K165R mutant forms of $p27^{Kip1}$ were incubated for the indicated times with a fraction of HEK293T cell extract from which proteasomes had been removed by ultracentrifugation (S100Pr−) as well as with an ATP-regenerating system, as described in the Methods section. The reaction mixtures were subjected to immunoblot analysis with anti-GST. The arrowhead indicates the position of unmodified GST-$p27^{Kip1}$. (D) The stability of HA-$p27^{Kip1}$ (WT or K165R) was monitored by treatment of transfected HEK293T cells with CHX for the indicated times followed by immunoblot analysis with anti-HA. (E) The band intensity corresponding to HA-$p27^{Kip1}$ (WT or K165R) in experiments similar to that in (D) was normalized by that of HSP90 and then expressed relative to the corresponding value for time zero. Data are means ± SEM for three independent experiments.

The identified ubiquitylated proteins include proteins that have previously been shown to be ubiquitylated such as histones H2A and H2B, β-catenin, hypoxia-inducible factor 1α (HIF1α), Bax, signal transducer and activator of transcription 5a (STAT5a), and ubiquitin itself. In addition to the ubiquitylation of all seven lysines of ubiquitin, we also detected ubiquitylation of the NH_2-terminal methionine of endogenous ubiquitin (Table 1), which participates in the formation of linear ubiquitin chains.[31,32]

dx.doi.org/10.1021/pr200668y | J. Proteome Res. 2012, 11, 796–807

Many important regulators of cell cycle progression were also found to be ubiquitylated in our analysis (Table 2). For example, CDK1 (also known as CDC2), CDK4, and CDK6 were ubiquitylated, as was the CDK inhibitor $p27^{Kip1}$. Of note, five of six MCM proteins (MCM2, -3, -4, -6, and -7), which form a complex to serve as the major replicative helicase and the licensing factor for DNA replication, were found to be ubiquitylated, some of them extensively so. Geminin, an inhibitor of DNA replication licensing factor Cdt1, was also included in the list. Although degradation of CDKs and CDK inhibitors, as well as that of MCM proteins and geminin, is thought to occur during different phases of the cell cycle, these proteins were simultaneously identified, probably because we used asynchronous cells for our analysis. The tumor suppressor p53 was also found to be ubiquitylated on lysines 120, 321, 357, and 370. Lysine at position 120 was previously shown to undergo acetylation but not ubiquitylation,[33,34] but our results now show that it is indeed ubiquitylated. Lysines are often targeted by protein modifications such as acetylation, methylation, ubiquitylation, SUMOylation, and neddylation.[35−42] Whereas these modifications have their own specific roles, one modification can competitively inhibit another and its associated function.[43−47] Our data set also contains many previously known ubiquitylation sites of proteins related to DNA damage and repair (Table 2). The K0-Ub conjugation system was expected to identify both mono- and polyubiquitylation sites in principle. Lysine at position 561 of Fanconi anemia group D2 protein (FANCD2) and Lys^{164} of proliferating cell nuclear antigen (PCNA), which have previously been identified as mono-ubiquitylation sites, were indeed detected by our method. We also identified a large number of novel ubiquitylation sites located on various proteins (Supplementary Table S2, Supporting Information).

Validation Study for Ubiquitylation of $p27^{Kip1}$ on Lys^{165}

To validate our MS data set, we evaluated the cellular function of an identified ubiquitylation site of the CDK inhibitor $p27^{Kip1}$, which is rapidly degraded by the ubiquitin−proteasome system at the G_1−S transition of the cell cycle in response to mitogenic signals.[48,49] Our MS data set contains a unique site (Lys^{165}) for ubiquitylation of $p27^{Kip1}$ (Figure 6A). We previously showed that the extent of $p27^{Kip1}$ ubiquitylation was markedly reduced when lysine residues at positions 134, 153, and 165 were all replaced with arginine, suggesting that one or more of these lysine residues is the target for ubiquitin conjugation.[50] We therefore replaced Lys^{165} of $p27^{Kip1}$ with arginine (K165R) and subjected the mutant protein to in vivo and in vitro ubiquitylation assays. These assays revealed that the level of ubiquitylation of the K165R mutant was greatly reduced compared with that of wild-type $p27^{Kip1}$ (Figure 6B,C). CHX chase analysis also showed that the K165R mutant was markedly more stable than wild-type $p27^{Kip1}$ (Figure 6D,E). This lysine residue therefore appears to be solely (or at least, largely) responsible for the degradation of $p27^{Kip1}$. We thus propose that our method can be applied to the identification of physiological ubiquitylation sites in a large number of proteins.

CONCLUSIONS

Although lysine ubiquitylation has been studied extensively over the past 30 years, only a limited number of ubiquitylation sites have been identified to date, and important questions regarding the entire ubiquitin system still remain unanswered. We have now established a method for the large-scale identification of ubiquitylation sites based on K0-Ub, and we have shown that this approach is able to identify in vivo ubiquitylation sites of ubiquitin−proteasome target proteins. Engineered ubiquitin (K0-Ub) is thus a powerful tool to identify biological ubiquitylation reactions. We have identified 1392 sites in 794 proteins in the present study. In conclusion, our data provide extensive insight into human ubiquitylation sites, together with novel information regarding the nature of ubiquitylation.

ASSOCIATED CONTENT

Supporting Information

The detailed information of identified peptides and proteins are listed in Supplementary Tables S1 and S2. The emPAI value of "top 2000" proteins from HEK293T cells are listed in Supplementary Table S3. This material is available free of charge via the Internet at http://pubs.acs.org.

AUTHOR INFORMATION

Corresponding Author

*Tel.: +81-92-642-6815. Fax: +81-92-642-6819. E-mail: nakayak1@bioreg.kyushu-u.ac.jp.

ACKNOWLEDGMENT

We thank M. Oda, E. Koba, T. Takami, and N. Nishimura for technical assistance, and A. Ohta for help in preparation of the manuscript. This work was supported in part by a grant from the Ministry of Education, Culture, Sports, Science, and Technology of Japan.

REFERENCES

(1) Hershko, A.; Ciechanover, A. The ubiquitin system. *Annu. Rev. Biochem.* **1998**, *67*, 425–479.

(2) Pickart, C. M. Mechanisms underlying ubiquitination. *Annu. Rev. Biochem.* **2001**, *70*, 503–533.

(3) Finley, D.; Ciechanover, A.; Varshavsky, A. Ubiquitin as a central cellular regulator. *Cell* **2004**, *116* (2 Suppl), S29–S322 p following S.

(4) Scheffner, M.; Nuber, U.; Huibregtse, J. M. Protein ubiquitination involving an E1-E2-E3 enzyme ubiquitin thioester cascade. *Nature* **1995**, *373* (6509), 81–83.

(5) Aebersold, R.; Mann, M. Mass spectrometry-based proteomics. *Nature* **2003**, *422* (6928), 198–207.

(6) Witze, E. S.; Old, W. M.; Resing, K. A.; Ahn, N. G. Mapping protein post-translational modifications with mass spectrometry. *Nat. Methods* **2007**, *4* (10), 798–806.

(7) Choudhary, C.; Mann, M. Decoding signalling networks by mass spectrometry-based proteomics. *Nat. Rev. Mol. Cell. Biol.* **2010**, *11* (6), 427–439.

(8) Marotti, L. A., Jr.; Newitt, R.; Wang, Y.; Aebersold, R.; Dohlman, H. G. Direct identification of a G protein ubiquitination site by mass spectrometry. *Biochemistry* **2002**, *41* (16), 5067–5074.

(9) Peng, J.; Schwartz, D.; Elias, J. E.; Thoreen, C. C.; Cheng, D.; Marsischky, G.; Roelofs, J.; Finley, D.; Gygi, S. P. A proteomics approach to understanding protein ubiquitination. *Nat. Biotechnol.* **2003**, *21* (8), 921–926.

(10) Xu, P.; Peng, J. Dissecting the ubiquitin pathway by mass spectrometry. *Biochim. Biophys. Acta* **2006**, *1764* (12), 1940–1947.

(11) Mayor, T.; Lipford, J. R.; Graumann, J.; Smith, G. T.; Deshaies, R. J. Analysis of polyubiquitin conjugates reveals that the Rpn10 substrate receptor contributes to the turnover of multiple proteasome targets. *Mol. Cell. Proteomics* **2005**, *4* (6), 741–751.

(12) Tagwerker, C.; Flick, K.; Cui, M.; Guerrero, C.; Dou, Y.; Auer, B.; Baldi, P.; Huang, L.; Kaiser, P. A tandem affinity tag for two-step

purification under fully denaturing conditions: application in ubiquitin profiling and protein complex identification combined with in vivocross-linking. *Mol. Cell. Proteomics* **2006**, *5* (4), 737–748.

(13) Meierhofer, D.; Wang, X.; Huang, L.; Kaiser, P. Quantitative analysis of global ubiquitination in HeLa cells by mass spectrometry. *J. Proteome Res.* **2008**, *7* (10), 4566–4576.

(14) Danielsen, J. M.; Sylvestersen, K. B.; Bekker-Jensen, S.; Szklarczyk, D.; Poulsen, J. W.; Horn, H.; Jensen, L. J.; Mailand, N.; Nielsen, M. L. Mass spectrometric analysis of lysine ubiquitylation reveals promiscuity at site level. *Mol. Cell. Proteomics* **2011**, *10* (3), M110 003590.

(15) Matsumoto, M.; Hatakeyama, S.; Oyamada, K.; Oda, Y.; Nishimura, T.; Nakayama, K. I. Large-scale analysis of the human ubiquitin-related proteome. *Proteomics* **2005**, *5* (16), 4145–4151.

(16) Vasilescu, J.; Smith, J. C.; Ethier, M.; Figeys, D. Proteomic analysis of ubiquitinated proteins from human MCF-7 breast cancer cells by immunoaffinity purification and mass spectrometry. *J. Proteome Res.* **2005**, *4* (6), 2192–2200.

(17) Newton, K.; Matsumoto, M. L.; Wertz, I. E.; Kirkpatrick, D. S.; Lill, J. R.; Tan, J.; Dugger, D.; Gordon, N.; Sidhu, S. S.; Fellouse, F. A.; Komuves, L.; French, D. M.; Ferrando, R. E.; Lam, C.; Compaan, D.; Yu, C.; Bosanac, I.; Hymowitz, S. G.; Kelley, R. F.; Dixit, V. M. Ubiquitin chain editing revealed by polyubiquitin linkage-specific antibodies. *Cell* **2008**, *134* (4), 668–678.

(18) Matsumoto, M. L.; Wickliffe, K. E.; Dong, K. C.; Yu, C.; Bosanac, I.; Bustos, D.; Phu, L.; Kirkpatrick, D. S.; Hymowitz, S. G.; Rape, M.; Kelley, R. F.; Dixit, V. M. K11-linked polyubiquitination in cell cycle control revealed by a K11 linkage-specific antibody. *Mol. Cell* **2010**, *39* (3), 477–484.

(19) Tan, F.; Lu, L.; Cai, Y.; Wang, J.; Xie, Y.; Wang, L.; Gong, Y.; Xu, B. E.; Wu, J.; Luo, Y.; Qiang, B.; Yuan, J.; Sun, X.; Peng, X. Proteomic analysis of ubiquitinated proteins in normal hepatocyte cell line Chang liver cells. *Proteomics* **2008**, *8* (14), 2885–96.

(20) Hjerpe, R.; Aillet, F.; Lopitz-Otsoa, F.; Lang, V.; England, P.; Rodriguez, M. S. Efficient protection and isolation of ubiquitylated proteins using tandem ubiquitin-binding entities. *EMBO Rep.* **2009**, *10* (11), 1250–1258.

(21) Shi, Y.; Chan, D. W.; Jung, S. Y.; Malovannaya, A.; Wang, Y.; Qin, J. A data set of human endogenous protein ubiquitination sites. *Mol. Cell. Proteomics* **2011**, *10* (5), M110002089.

(22) Xu, G.; Paige, J. S.; Jaffrey, S. R. Global analysis of lysine ubiquitination by ubiquitin remnant immunoaffinity profiling. *Nat. Biotechnol.* **2010**, *28* (8), 868–873.

(23) Nishiyama, M.; Oshikawa, K.; Tsukada, Y.; Nakagawa, T.; Iemura, S.; Natsume, T.; Fan, Y.; Kikuchi, A.; Skoultchi, A. I.; Nakayama, K. I. CHD8 suppresses p53-mediated apoptosis through histone H1 recruitment during early embryogenesis. *Nat. Cell Biol.* **2009**, *11* (2), 172–182.

(24) Oshikawa, K.; Matsumoto, M.; Yada, M.; Kamura, T.; Hatakeyama, S.; Nakayama, K. I. Preferential interaction of TIP120A with Cul1 that is not modified by NEDD8 and not associated with Skp1. *Biochem. Biophys. Res. Commun.* **2003**, *303* (4), 1209–1216.

(25) Rappsilber, J.; Mann, M.; Ishihama, Y. Protocol for micro-purification, enrichment, pre-fractionation and storage of peptides for proteomics using StageTips. *Nat. Protoc.* **2007**, *2* (8), 1896–1906.

(26) Ishihama, Y.; Oda, Y.; Tabata, T.; Sato, T.; Nagasu, T.; Rappsilber, J.; Mann, M. Exponentially modified protein abundance index (emPAI) for estimation of absolute protein amount in proteomics by the number of sequenced peptides per protein. *Mol. Cell. Proteomics* **2005**, *4* (9), 1265–1272.

(27) Shinoda, K.; Tomita, M.; Ishihama, Y. emPAI Calc--for the estimation of protein abundance from large-scale identification data by liquid chromatography-tandem mass spectrometry. *Bioinformatics* **2010**, *26* (4), 576–577.

(28) Hatakeyama, S.; Yada, M.; Matsumoto, M.; Ishida, N.; Nakayama, K. I. U box proteins as a new family of ubiquitin-protein ligases. *J. Biol. Chem.* **2001**, *276* (35), 33111–33120.

(29) Ziv, I.; Matiuhin, Y.; Kirkpatrick, D. S.; Erpapazoglou, Z.; Leon, S.; Pantazopoulou, M.; Kim, W.; Gygi, S. P.; Haguenauer-Tsapis, R.; Reis, N.; Glickman, M. H.; Kleifeld, O. A perturbed ubiquitin landscape distinguishes between ubiquitin in trafficking and in proteolysis. *Mol. Cell. Proteomics* **2011**, *10* (5), M111009753.

(30) Semple, C. A. The comparative proteomics of ubiquitination in mouse. *Genome Res.* **2003**, *13* (6B), 1389–1394.

(31) Kirisako, T.; Kamei, K.; Murata, S.; Kato, M.; Fukumoto, H.; Kanie, M.; Sano, S.; Tokunaga, F.; Tanaka, K.; Iwai, K. A ubiquitin ligase complex assembles linear polyubiquitin chains. *EMBO J.* **2006**, *25* (20), 4877–4887.

(32) Tokunaga, F.; Sakata, S.; Saeki, Y.; Satomi, Y.; Kirisako, T.; Kamei, K.; Nakagawa, T.; Kato, M.; Murata, S.; Yamaoka, S.; Yamamoto, M.; Akira, S.; Takao, T.; Tanaka, K.; Iwai, K. Involvement of linear polyubiquitylation of NEMO in NF-κB activation. *Nat. Cell Biol.* **2009**, *11* (2), 123–132.

(33) Kruse, J. P.; Gu, W. Modes of p53 regulation. *Cell* **2009**, *137* (4), 609–622.

(34) Charvet, C.; Wissler, M.; Brauns-Schubert, P.; Wang, S. J.; Tang, Y.; Sigloch, F. C.; Mellert, H.; Brandenburg, M.; Lindner, S. E.; Breit, B.; Green, D. R.; McMahon, S. B.; Borner, C.; Gu, W.; Maurer, U. Phosphorylation of Tip60 by GSK-3 determines the induction of PUMA and apoptosis by p53. *Mol. Cell* **2011**, *42* (5), 584–96.

(35) Johnson, E. S. Protein modification by SUMO. *Annu. Rev. Biochem.* **2004**, *73*, 355–382.

(36) Choudhary, C.; Kumar, C.; Gnad, F.; Nielsen, M. L.; Rehman, M.; Walther, T. C.; Olsen, J. V.; Mann, M. Lysine acetylation targets protein complexes and co-regulates major cellular functions. *Science* **2009**, *325* (5942), 834–840.

(37) Gareau, J. R.; Lima, C. D. The SUMO pathway: emerging mechanisms that shape specificity, conjugation and recognition. *Nat. Rev. Mol. Cell. Biol.* **2010**, *11* (12), 861–871.

(38) Perry, A. S.; Watson, R. W.; Lawler, M.; Hollywood, D. The epigenome as a therapeutic target in prostate cancer. *Nat. Rev. Urol.* **2010**, *7* (12), 668–680.

(39) Wang, Q.; Zhang, Y.; Yang, C.; Xiong, H.; Lin, Y.; Yao, J.; Li, H.; Xie, L.; Zhao, W.; Yao, Y.; Ning, Z. B.; Zeng, R.; Xiong, Y.; Guan, K. L.; Zhao, S.; Zhao, G. P. Acetylation of metabolic enzymes coordinates carbon source utilization and metabolic flux. *Science* **2010**, *327* (5968), 1004–1007.

(40) Zhao, S.; Xu, W.; Jiang, W.; Yu, W.; Lin, Y.; Zhang, T.; Yao, J.; Zhou, L.; Zeng, Y.; Li, H.; Li, Y.; Shi, J.; An, W.; Hancock, S. M.; He, F.; Qin, L.; Chin, J.; Yang, P.; Chen, X.; Lei, Q.; Xiong, Y.; Guan, K. L. Regulation of cellular metabolism by protein lysine acetylation. *Science* **2010**, *327* (5968), 1000–1004.

(41) Margueron, R.; Reinberg, D. The Polycomb complex PRC2 and its mark in life. *Nature* **2011**, *469* (7330), 343–349.

(42) Watson, I. R.; Irwin, M. S.; Ohh, M. NEDD8 pathways in cancer, Sine Quibus Non. *Cancer Cell* **2011**, *19* (2), 168–176.

(43) Desterro, J. M.; Rodriguez, M. S.; Hay, R. T. SUMO-1 modification of IκBα inhibits NF-κB activation. *Mol. Cell* **1998**, *2* (2), 233–239.

(44) Kouzarides, T. Acetylation: a regulatory modification to rival phosphorylation? *EMBO J.* **2000**, *19* (6), 1176–1179.

(45) Papouli, E.; Chen, S.; Davies, A. A.; Huttner, D.; Krejci, L.; Sung, P.; Ulrich, H. D. Crosstalk between SUMO and ubiquitin on PCNA is mediated by recruitment of the helicase Srs2p. *Mol. Cell* **2005**, *19* (1), 123–133.

(46) Yang, X. J.; Seto, E. Lysine acetylation: codified crosstalk with other posttranslational modifications. *Mol. Cell* **2008**, *31* (4), 449–461.

(47) Wu, S. Y.; Chiang, C. M. Crosstalk between sumoylation and acetylation regulates p53-dependent chromatin transcription and DNA binding. *EMBO J.* **2009**, *28* (9), 1246–1259.

(48) Pagano, M.; Tam, S. W.; Theodoras, A. M.; Beer-Romero, P.; Del Sal, G.; Chau, V.; Yew, P. R.; Draetta, G. F.; Rolfe, M. Role of the ubiquitin-proteasome pathway in regulating abundance of the cyclin-dependent kinase inhibitor p27. *Science* **1995**, *269* (5224), 682–685.

(49) Nakayama, K. I.; Nakayama, K. Ubiquitin ligases: cell-cycle control and cancer. *Nat. Rev. Cancer* **2006**, *6* (5), 369–381.

(50) Shirane, M.; Harumiya, Y.; Ishida, N.; Hirai, A.; Miyamoto, C.; Hatakeyama, S.; Nakayama, K. I.; Kitagawa, M. Down-regulation of $p27^{Kip1}$ by two mechanisms, ubiquitin-mediated degradation and proteolytic processing. *J. Biol. Chem.* **1999**, *274* (20), 13886–13893.

Research article

Fbxw7 regulates lipid metabolism and cell fate decisions in the mouse liver

Ichiro Onoyama,[1,2] Atsushi Suzuki,[3,4] Akinobu Matsumoto,[1,2] Kengo Tomita,[5] Hideki Katagiri,[6] Yuichi Oike,[4,7] Keiko Nakayama,[2,8] and Keiichi I. Nakayama[1,2]

[1]Department of Molecular and Cellular Biology, Medical Institute of Bioregulation, Kyushu University, Higashi-ku, Fukuoka, Fukuoka, Japan. [2]CREST, Japan Science and Technology Agency, Kawaguchi, Saitama, Japan. [3]Division of Organogenesis and Regeneration, Medical Institute of Bioregulation, Kyushu University, Higashi-ku, Fukuoka, Fukuoka, Japan. [4]PRESTO, Japan Science and Technology Agency, Kawaguchi, Saitama, Japan. [5]Division of Gastroenterology and Hepatology, Department of Internal Medicine, National Defense Medical College, Tokorozawa, Saitama, Japan. [6]Division of Advanced Therapeutics for Metabolic Diseases, Center for Translational and Advanced Animal Research, Tohoku University Graduate School of Medicine, Sendai, Japan. [7]Department of Molecular Genetics, Graduate School of Medical Sciences, Kumamoto University, Kumamoto, Japan. [8]Division of Developmental Genetics, Center for Translational and Advanced Animal Research, Tohoku University Graduate School of Medicine, Sendai, Japan.

E3 ubiquitin ligase complexes of the SCF type consist of ring-box 1 (Rbx1), cullin 1 (Cul1), S-phase kinase-associated protein 1 (Skp1), and a member of the F-box family of proteins. The identity of the F-box protein determines the substrate specificity of the complex. The F-box family member F-box- and WD repeat domain–containing 7 (Fbxw7; also known as Fbw7, SEL-10, hCdc4, and hAgo) targets for degradation proteins with wide-ranging functions, and uncovering its in vivo role has been difficult, because *Fbxw7*$^{-/-}$ embryos die in utero. Using two different Cre-loxP systems (*Mx1*-Cre and *Alb*-Cre), we generated mice with liver-specific null mutations of *Fbxw7*. Hepatic ablation of *Fbxw7* resulted in hepatomegaly and steatohepatitis, with massive deposition of triglyceride, a phenotype similar to that observed in humans with nonalcoholic steatohepatitis. Both cell proliferation and the abundance of Fbxw7 substrates were increased in the Fbxw7-deficient liver. Long-term Fbxw7 deficiency resulted in marked proliferation of the biliary system and the development of hamartomas. Fbxw7 deficiency also skewed the differentiation of liver stem cells toward the cholangiocyte lineage rather than the hepatocyte lineage in vitro. This bias was corrected by additional loss of the Notch cofactor RBP-J, suggesting that Notch accumulation triggered the abnormal proliferation of the biliary system. Together, our results suggest that Fbxw7 plays key roles, regulating lipogenesis and cell proliferation and differentiation in the liver.

Introduction

The abundance of cellular proteins is regulated in a coordinated manner at the levels of their synthesis and degradation. In particular, intracellular proteolysis is thought to be subject to highly specific regulation. The ubiquitin-proteasome system is responsible for such specific degradation of proteins, with ubiquitylation playing the regulatory role in this process. Ubiquitylation of target proteins is mediated by the sequential action of 3 enzymes: a ubiquitin-activating enzyme (E1), a ubiquitin-conjugating enzyme (E2), and a ubiquitin ligase (E3). The ubiquitylated substrates are then selectively recognized and degraded by the 26S proteasome (1). Uncontrolled proteolysis is implicated in dysregulation of cell proliferation and aberrant cell differentiation and is thought to underlie many human malignancies (2).

F-box proteins determine the substrate specificity of the SCF-type E3 complex, which consists of the RING-finger protein ring-box 1 (Rbx1; also known as Roc1 and Hrt1), the scaffold protein cullin 1 (Cul1), and the adaptor protein S-phase kinase-associated protein 1 (Skp1) in addition to an F-box protein (2–4). F-box- and WD repeat domain–containing 7 (Fbxw7; also known as Fbw7, SEL-10, hCdc4, and hAgo) is a member of the F-box protein family that was initially identified as a negative regulator of LIN-12–mediated (Notch-mediated) signaling in *Caenorhabditis elegans* by genetic analysis (5, 6). Fbxw7 also interacts with Notch family proteins and promotes their ubiquitin-dependent turnover in mammalian cells (5, 7, 8). Furthermore, it targets for degradation various mammalian proteins that control cell cycle progression (2, 4), including cyclin E (9–11), c-Myc (12, 13), and c-Jun (14, 15), as well as other proteins that do not contribute directly to cell cycle control, such as SREBPs (16–18), mammalian target of rapamycin (mTOR) (19), and PPAR-γ coactivator-1α (PGC-1α) (20).

Given its ability to promote degradation of cyclin E, c-Myc, c-Jun, and Notch, all of which are products of proto-oncogenes, Fbxw7 was expected to function as an oncosuppressor protein. Indeed, mutations in the *Fbxw7* gene have been detected in many types of human malignancy, including cholangiocarcinoma and T cell acute lymphoblastic leukemia as well as pancreatic, gastric, colorectal, prostate, and endometrial cancer (21–31). The study of Fbxw7 is thus important not only from the point of view of basic biology but also from the medical standpoint.

To analyze the functions of Fbxw7 in vivo, we and others have generated Fbxw7-deficient mice. However, *Fbxw7*$^{-/-}$ embryos were found to die in utero at E10.5, manifesting marked abnormalities in vascular development as a result of dysregulation of Notch signaling (32, 33). To avoid this early embryonic mortality, we have established mice in which *Fbxw7* is conditionally disrupted in T cells (34) or in hematopoietic stem cells (35), and we have also examined the effects of *Fbxw7* ablation in mouse embryonic fibroblasts (36). The loss of Fbxw7 in immature T cells results in the failure of these cells to exit the cell cycle, leading to thymic hyperplasia and the subsequent development of lymphoma. Among known targets of Fbxw7, only c-Myc and Notch accumulated in the Fbxw7-deficient thymocytes, and c-Myc accumulation was found

Conflict of interest: The authors have declared that no conflict of interest exists.
Citation for this article: *J Clin Invest.* 2010;121(1):342–354. doi:10.1172/JCI40725.

to be primarily responsible for the hyperproliferation phenotype. In contrast to that in immature T cells, the accumulation of c-Myc apparent in Fbxw7-null mature T cells induced expression of p53, which in turn led to cell cycle arrest and apoptosis. Furthermore, we found that Fbxw7 contributes to the long-term maintenance of hematopoietic stem cells. Most of the phenotypes of Fbxw7 deficiency in these conditional mouse mutants are related to cell proliferation or death and appear to be attributable to deregulation of c-Myc and Notch. Although Fbxw7 targets many substrates that do not participate directly in cell cycle control for degradation, the physiological roles of Fbxw7-mediated degradation of such targets have been largely unclear.

We have now examined the consequences of Fbxw7 deficiency in the liver. Unexpectedly, the major phenotypes associated with such deficiency were abnormalities in lipid metabolism and cell differentiation, which differ markedly from those in hematopoietic cell lineages and fibroblasts, in which Fbxw7 contributes primarily to the control of cell proliferation and apoptosis. We thus propose that Fbxw7 targets different groups of proteins for ubiquitin-dependent degradation and thereby contributes to distinct biological functions in a tissue-specific manner.

Results

Conditional inactivation of Fbxw7 in the liver by 2 Cre-loxP systems. We generated mice harboring floxed *Fbxw7* alleles (referred to herein as *Fbxw7*$^{F/F}$ mice) in which exon 5 (which encodes the F-box domain) is flanked by loxP sites (34). To ablate *Fbxw7* in the liver, we crossed these *Fbxw7*$^{F/F}$ mice with mice harboring a Cre transgene under the control of the promoter for the myxovirus resistance 1 (*Mx1*) or albumin (*Alb*) genes (*Mx1*-Cre or *Alb*-Cre mice). We confirmed that almost all floxed alleles were inactivated by Cre recombinase in the livers of *Alb*-Cre/*Fbxw7*$^{F/F}$ mice as well as in those of *Mx1*-Cre/*Fbxw7*$^{F/F}$ mice at 3 weeks after the last of 3 i.p. injections of poly(I)-poly(C) (pIpC) to activate the *Mx1* gene promoter (Figure 1A). For subsequent experiments, we examined the effects of short- or long-term Fbxw7 deficiency in *Mx1*-Cre/*Fbxw7*$^{F/F}$ mice and those of long-term a priori deficiency in *Alb*-Cre/*Fbxw7*$^{F/F}$ mice.

Massive lipid deposition and nonalcoholic steatohepatitis–like lesions in the Fbxw7-deficient liver. *Mx1*-Cre/*Fbxw7*$^{F/F}$ mice at 8 weeks of age were subjected to i.p. injection of pIpC every other day for 3 days to activate the *Mx1* gene promoter. At 3 weeks after the last injection of pIpC, the livers of these mice were enlarged and lighter in color compared with those of control animals (Figure 1B). The liver-to-body weight ratio of these *Mx1*-Cre/*Fbxw7*$^{F/F}$ mice was increased by approximately 30% relative to that of control mice (Figure 1C). Histological examination revealed that the nuclei of cells in the enlarged liver remained centrally located, whereas the corresponding cytoplasm was only weakly eosinophilic and contained numerous microvesicular vacuoles (Figure 1, D and E). Staining with Oil red O (Figure 1, F–I) also revealed massive lipid deposition, predominantly in the area around central veins (Figure 1G). Similar lipid deposition was also observed in the livers of *Alb*-Cre/*Fbxw7*$^{F/F}$ mice at as early as 12 weeks of age (Figure 1, J and K). The mechanism underlying such an uneven localization of lipid deposition is unclear and awaits further investigation.

Lobular infiltration of inflammatory cells such as lymphocytes and neutrophils (Figure 1, L and M; arrowhead), as well as the presence of many ballooned hepatocytes (occasionally containing Mallory body–like eosinophilic inclusions) (Figure 1, N and O; arrow), were observed in the livers of older mutant mice at approximately 50 weeks of age. Sinusoidal fibrogenic changes in the liver as revealed by Masson's trichrome staining were also evident (Figure 1, P and Q), and serum levels of aspartate aminotransferase (AST) and alanine aminotransferase (ALT) were significantly increased (Figure 1R) in *Alb*-Cre/*Fbxw7*$^{F/F}$ mice at 50 weeks of age. The serum level of bilirubin tended to be higher in the mutant animals than in age-matched controls, suggestive of the destruction of liver tissue in the mutant mice, although this difference was not statistically significant (Supplemental Figure 1; supplemental material available online with this article; doi:10.1172/JCI40725DS1). The onset of inflammatory changes occurred later than that of steatosis, but feeding *Mx1*-Cre/*Fbxw7*$^{F/F}$ mice a methionine- and choline-deficient (MCD) diet resulted in acceleration of inflammation (Figure 2A). The extents of steatosis and hepatitis were less pronounced in *Alb*-Cre/*Fbxw7*$^{F/F}$ mice than in *Mx1*-Cre/*Fbxw7*$^{F/F}$ mice subjected to acute ablation of Fbxw7, probably as a result of compensatory mechanisms operative during development in the former animals. However, massive steatosis and inflammation were also apparent in *Alb*-Cre/*Fbxw7*$^{F/F}$ mice fed the MCD diet, whereas control animals did not show such marked changes (Figure 2B). These results suggested that *Alb*-Cre/*Fbxw7*$^{F/F}$ mice are also more sensitive to steatohepatitis than are controls. The histological findings in both types of Fbxw7-deficient mice are highly similar to those associated with nonalcoholic steatohepatitis (NASH) in humans (37).

Expression of adipogenic and lipogenic genes in the Fbxw7-deficient liver. We next determined lipid concentrations in liver extracts. Triglyceride levels were significantly increased in the livers of *Mx1*-Cre/*Fbxw7*$^{F/F}$ mice compared with those in control animals at 3 weeks after the final pIpC injection, whereas the concentration of total cholesterol was not affected in the mutant livers (Figure 3A). Given that triglyceride synthesis is regulated predominantly by transcriptional activators, such as SREBPs, carbohydrate response element–binding protein (ChREBP), and PPAR-γ, we examined the expression of these proteins and their downstream targets in the liver. Immunoblot analysis revealed that the abundance of nuclear SREBP1, which is the major SREBP in the liver and a target of Fbxw7-mediated proteolysis (16, 17), was increased both in pIpC-injected *Mx1*-Cre/*Fbxw7*$^{F/F}$ mice and in *Alb*-Cre/*Fbxw7*$^{F/F}$ mice (Figure 3B and Supplemental Figure 2). The intensity of the more slowly migrating band, likely corresponding to the phosphorylated form of SREBP1, was especially increased, consistent with the previous observation that the phosphorylated forms of SREBPs are targeted by Fbxw7 (16–18), as is generally the case for Fbxw7 substrates (11, 34). In contrast, the amounts of ChREBP and PPAR-γ were decreased in the mutant mice compared with those in control animals, suggestive of the operation of a negative feedback loop triggered by triglyceride accumulation. Consistent with this notion, the abundance of *Pparg* mRNA in the liver was increased in SREBP cleavage–activating protein–deficient mice, in which the SREBP pathway is inactivated (38). The levels of PGC-1α and mTOR (total or phosphorylated forms) were unaffected by hepatic deletion of *Fbxw7*.

RT and real-time PCR analysis revealed that the abundance of mRNAs for the adipogenic and lipogenic transcriptional activators *SREBP1c*, *ChREBP*, and *Pparg* was decreased in the Fbxw7-deficient liver (Figure 3C), suggesting that the transcription of these genes is suppressed by a negative feedback loop triggered by the high level of triglyceride. At the protein level, the precursor form of SREBP1 was reduced, probably as a result of the decrease in the abundance of its mRNA, whereas the mature cleaved form was increased (Supplemental Figure 3). Among the downstream targets of SREBPs,

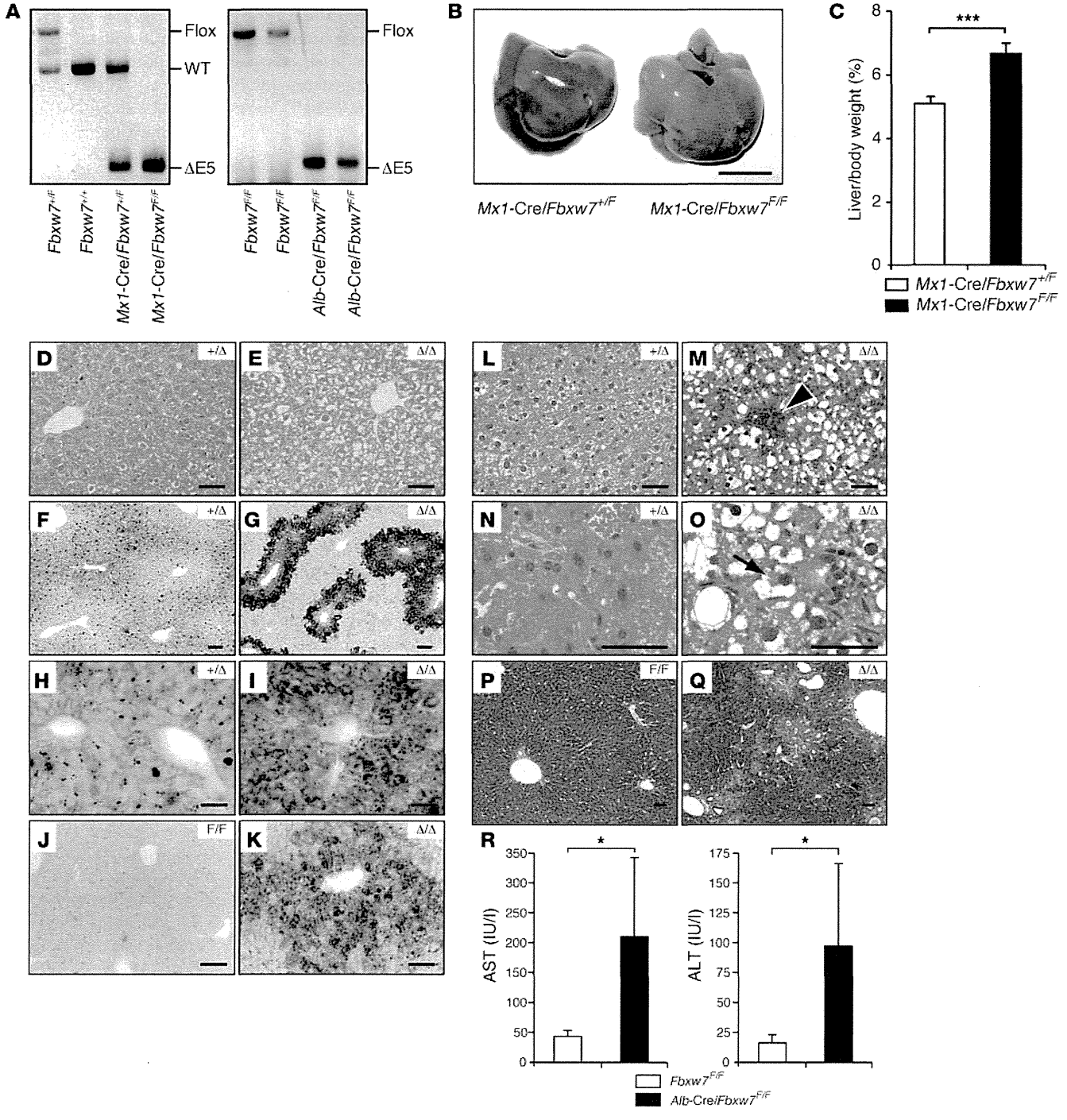

Figure 1

Development of NASH-like liver disease as a result of Fbxw7 deletion. (**A**) Genomic PCR analysis from the mouse liver of the indicated genotypes. The positions of amplified fragments corresponding to WT, floxed, and exon 5–deleted (ΔE5) alleles are indicated. (**B**) Gross appearance of the livers of indicated genotypes treated as in **A**. Scale bar: 10 mm. (**C**) Liver/body weight ratio of mice treated as in **A**. Data are mean ± SD from 5 animals of each genotype. ***$P < 0.005$. (**D** and **E**) H&E staining of liver sections from *Mx1*-Cre/*Fbxw7*$^{+/F}$ (+/Δ) and *Mx1*-Cre/*Fbxw7*$^{F/F}$ (Δ/Δ) mice, respectively, treated as in **A**. (**F** and **G**) Oil red O staining of liver sections treated as in **A**. (**H** and **I**) Higher-magnification views of images in **F** and **G**, respectively. (**J** and **K**) Oil red O staining of liver sections from *Fbxw7*$^{F/F}$ (F/F) and *Alb*-Cre/*Fbxw7*$^{F/F}$ (Δ/Δ) mice, respectively, at 12 weeks of age. (**L**–**O**) H&E staining of liver sections from *Mx1*-Cre/*Fbxw7*$^{+/F}$ (+/Δ) (**L** and **N**) and *Mx1*-Cre/*Fbxw7*$^{F/F}$ (Δ/Δ) (**M** and **O**) mice at 50 weeks after the final injection of pIpC. Lobular infiltration of inflammatory cells is indicated by the arrowhead, and Mallory body–like eosinophilic inclusion is indicated by the arrow. (**P** and **Q**) Masson's trichrome staining of liver sections from *Fbxw7*$^{F/F}$ (F/F) and *Alb*-Cre/*Fbxw7*$^{F/F}$ (Δ/Δ) mice, respectively, at 50 weeks of age. Scale bar: 50 μm (**D**, **E**, **H**, **I**, and **L**–**O**); 100 μm (**F**, **G**, **J**, **K**, **P**, and **Q**). (**R**) Serum AST and ALT activities in *Fbxw7*$^{F/F}$ ($n = 6$) and *Alb*-Cre/*Fbxw7*$^{F/F}$ ($n = 10$) mice at 50 weeks of age. Data are mean ± SD. *$P < 0.05$.

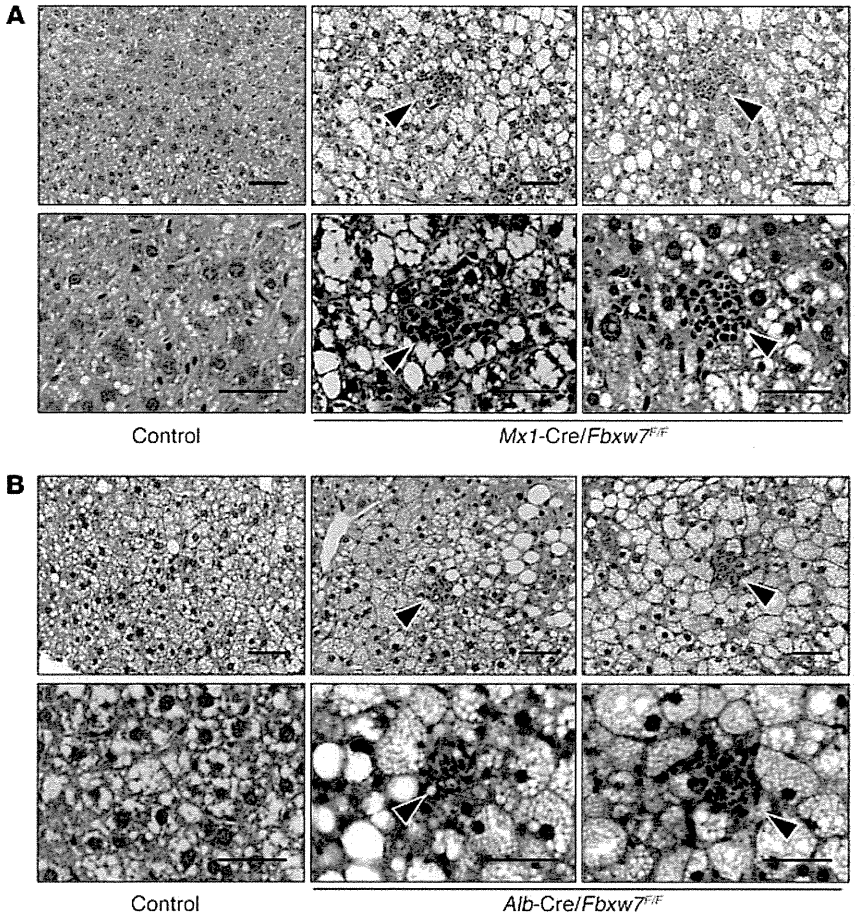

Figure 2
Increased susceptibility to a NASH-like condition conferred by Fbxw7 ablation in the liver. (**A**) *Mx1*-Cre/*Fbxw7*$^{+/F}$ (control) and *Mx1*-Cre/*Fbxw7*$^{F/F}$ mice were injected with pIpC at 8 weeks of age and then fed an MCD diet for 2 weeks. Liver sections were then subjected to H&E staining. Lower- and higher-magnification views are shown (top and bottom panels, respectively). In addition to fatty degeneration, many foci of lobular infiltration of inflammatory cells (arrowheads) were apparent in the livers of *Mx1*-Cre/*Fbxw7*$^{F/F}$ mice. Scale bar: 50 μm. (**B**) *Alb*-Cre/*Fbxw7*$^{+/F}$ (control) and *Alb*-Cre/*Fbxw7*$^{F/F}$ mice at 12 weeks of age were fed an MCD diet for 4 weeks and then analyzed as in **A**. Lower- and higher-magnification views are shown (top and bottom panels, respectively). Control mice developed a small extent of fatty degeneration, whereas *Alb*-Cre/*Fbxw7*$^{F/F}$ mice showed massive accumulation of lipid droplets and many foci of lobular infiltration of inflammatory cells (arrowheads) similar to those apparent in *Mx1*-Cre/*Fbxw7*$^{F/F}$ mice. Scale bar: 50 μm.

the amounts of mRNAs for fatty acid synthase (*Fas*) and stearoyl-CoA desaturase–1 (*Scd1*) were increased, whereas those for the LDL receptor (*Ldlr*) and HMG-CoA synthase (*Hmgcs1*) were decreased, in the mutant liver (Figure 3C). Immunostaining also showed that SREBP1 accumulated in the region around the central veins (Figure 3D), corresponding to the area of lipid deposition, even though deletion of *Fbxw7* appears to occur throughout almost the entire liver. The expression of SCD-1 was also increased in the region around the central veins in which SREBP1 was upregulated (Figure 3E). Collectively, these results suggested that the accumulation of SREBP proteins as a result of Fbxw7 ablation results in triglyceride deposition in the liver, which in turn affects the expression of other adipogenic and lipogenic genes as well as their downstream targets via a negative feedback loop.

Increased proliferation of Fbxw7-deficient hepatocytes. We compared the abundance of cyclin E and c-Myc between the livers of *Mx1*-Cre/*Fbxw7*$^{+/F}$ and *Mx1*-Cre/*Fbxw7*$^{F/F}$ mice at 3 or 50 weeks after the final pIpC injection, beginning at 8 weeks of age. Immunoblot analysis revealed that the amount of cyclin E in the livers of *Mx1*-Cre/*Fbxw7*$^{F/F}$ mice was increased compared with that in *Mx1*-Cre/*Fbxw7*$^{+/F}$ mice at 3 weeks after pIpC injection but not at 50 weeks (Figure 4A). The abundance of c-Myc was not affected by the loss of Fbxw7 in the liver, at either 3 or 50 weeks after injection. To measure the rate of hepatocyte proliferation, we subjected *Mx1*-Cre/*Fbxw7*$^{+/F}$ and *Mx1*-Cre/*Fbxw7*$^{F/F}$ mice to i.p. injection with BrdU for 3 consecutive days, beginning at 3 or 50 weeks after the final pIpC injection. Immunostaining of the liver with antibodies to BrdU at 1 day after the last BrdU injection revealed that the rate of BrdU incorporation was markedly increased in Fbxw7-deficient liver cells compared with that in control cells (Figure 4B). Most of the BrdU-positive cells were also reactive with antibodies to albumin but not with those to cytokeratin 19 (CK19) at 3 weeks after pIpC injection (Figure 4C), suggesting that the proliferating cells are predominantly hepatocytes. In contrast, at 50 weeks after pIpC injection, both hepatocytes and cholangiocytes in *Mx1*-Cre/*Fbxw7*$^{F/F}$ mice incorporated BrdU to a greater extent than did those in control mice. The TUNEL assay revealed that the frequency of apoptosis was also increased in the Fbxw7-deficient liver at 3 weeks after pIpC injection (Figure 4, D and E), suggesting that the loss of Fbxw7 transiently promotes cell cycle progression but eventually results in apoptosis in the liver, as it does in T lymphocytes (34).

Development of hamartomas with hyperproliferation of the biliary system in the Fbxw7-deficient liver. We next examined in more detail the long-term effects of Fbxw7 loss in the liver. Macroscopic examination of *Mx1*-Cre/*Fbxw7*$^{F/F}$ mice at 50 weeks after pIpC injection at 8 weeks of age revealed that the mutant liver was enlarged and darker in color compared with the control liver and possessed a rough surface as a result of the presence of several nodules (Figure 5A). We confirmed that the *Fbxw7* gene was deleted in such nodules (Figure 5B), which were grossly demarcated and readily excised from the liver. Histological examination revealed structural abnormalities characterized by marked dilation of intrahepatic bile ducts as well as apparent proliferation of the biliary system

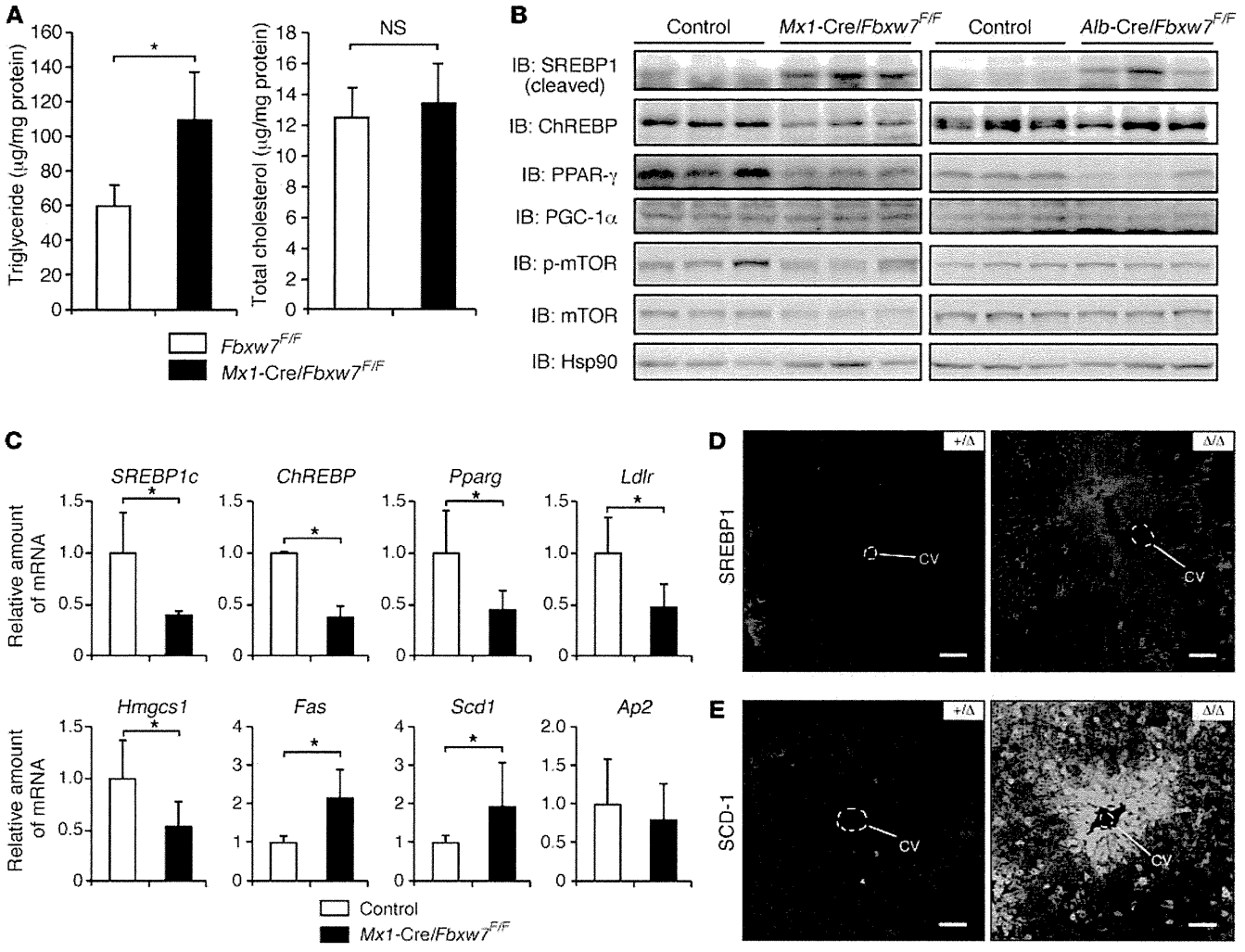

Figure 3

Deposition of triglyceride and accumulation of SREBP1 in the Fbxw7-deficient liver. (**A**) Triglyceride and total cholesterol concentrations in the livers of *Mx1*-Cre/*Fbxw7*$^{+/F}$ (control) and *Mx1*-Cre/*Fbxw7*$^{F/F}$ mice at 3 weeks after the final injection of pIpC, beginning at 8 weeks of age. Data are mean ± SD from 3 mice of each genotype. *$P < 0.05$. (**B**) Protein extracts of the livers of *Mx1*-Cre/*Fbxw7*$^{+/F}$ (control) and *Mx1*-Cre/*Fbxw7*$^{F/F}$ mice at 3 weeks after the final injection of pIpC, beginning at 8 weeks of age, were subjected to IB analysis with antibodies to the indicated proteins (left panel). Liver extracts of *Fbxw7*$^{F/F}$ (control) and *Alb*-Cre/*Fbxw7*$^{F/F}$ mice at 12 weeks of age were similarly analyzed (right panel). Three animals were examined for each genotype. Hsp90 was analyzed as a loading control. p-mTOR, phosphorylated mTOR. (**C**) RT and real-time PCR analysis of the indicated mRNAs in the livers of *Mx1*-Cre/*Fbxw7*$^{+/F}$ (control) and *Mx1*-Cre/*Fbxw7*$^{F/F}$ mice treated as in **A**. Normalized data are expressed relative to the corresponding value for control mice and are mean ± SD from 3 independent experiments. *$P < 0.05$. (**D** and **E**) Liver sections of *Mx1*-Cre/*Fbxw7*$^{+/F}$ (+/Δ) and *Mx1*-Cre/*Fbxw7*$^{F/F}$ (Δ/Δ) mice, treated as in **A**, were subjected to immunofluorescence staining with antibodies (**D**) to SREBP1 and (**E**) to SCD-1. CV, central vein. Scale bar: 100 μm.

(Figure 5, C–F); these abnormalities were pathologically diagnosed as hamartomas. Such lesions were also observed, albeit to a lesser extent, in *Alb*-Cre/*Fbxw7*$^{F/F}$ mice at as early as 12 weeks of age (Figure 5, G and H). Hamartomas, which are reactive with antibodies to CK19 (Figure 5, I and J), developed in all mutant mice of both genotypes examined ($n = 14$). These results suggested that the loss of Fbxw7 may promote proliferation of the biliary system and shift the development of hepatic stem cells toward the cholangiocyte lineage rather than the hepatocyte lineage.

We examined the abundance of mRNAs for *Alb* (Figure 5K) and *CK19* (Figure 5L) as markers of hepatocyte and cholangiocyte lineages, respectively. The amount of *CK19* mRNA in the liver was increased as early as 2 weeks after pIpC injection in *Mx1*-Cre/*Fbxw7*$^{F/F}$ mice and showed a more than 40-fold increase at 50 weeks after *Fbxw7* deletion. In contrast, the abundance of *Alb* mRNA in the mutant liver at 50 weeks after pIpC injection was decreased by 40% compared with that in control liver. These changes in differentiation markers were thus consistent with a marked proliferation of the biliary system in the Fbxw7-deficient liver.

Skewed hepatic differentiation induced by Notch1 accumulation in the Fbxw7-deficient liver. The hepatic cell fate decision is thought to be largely dependent on Notch signaling (39–44). We therefore examined the expression of Notch, a target of Fbxw7, in the Fbxw7-deficient liver. Although immunoblot analysis did not reveal an

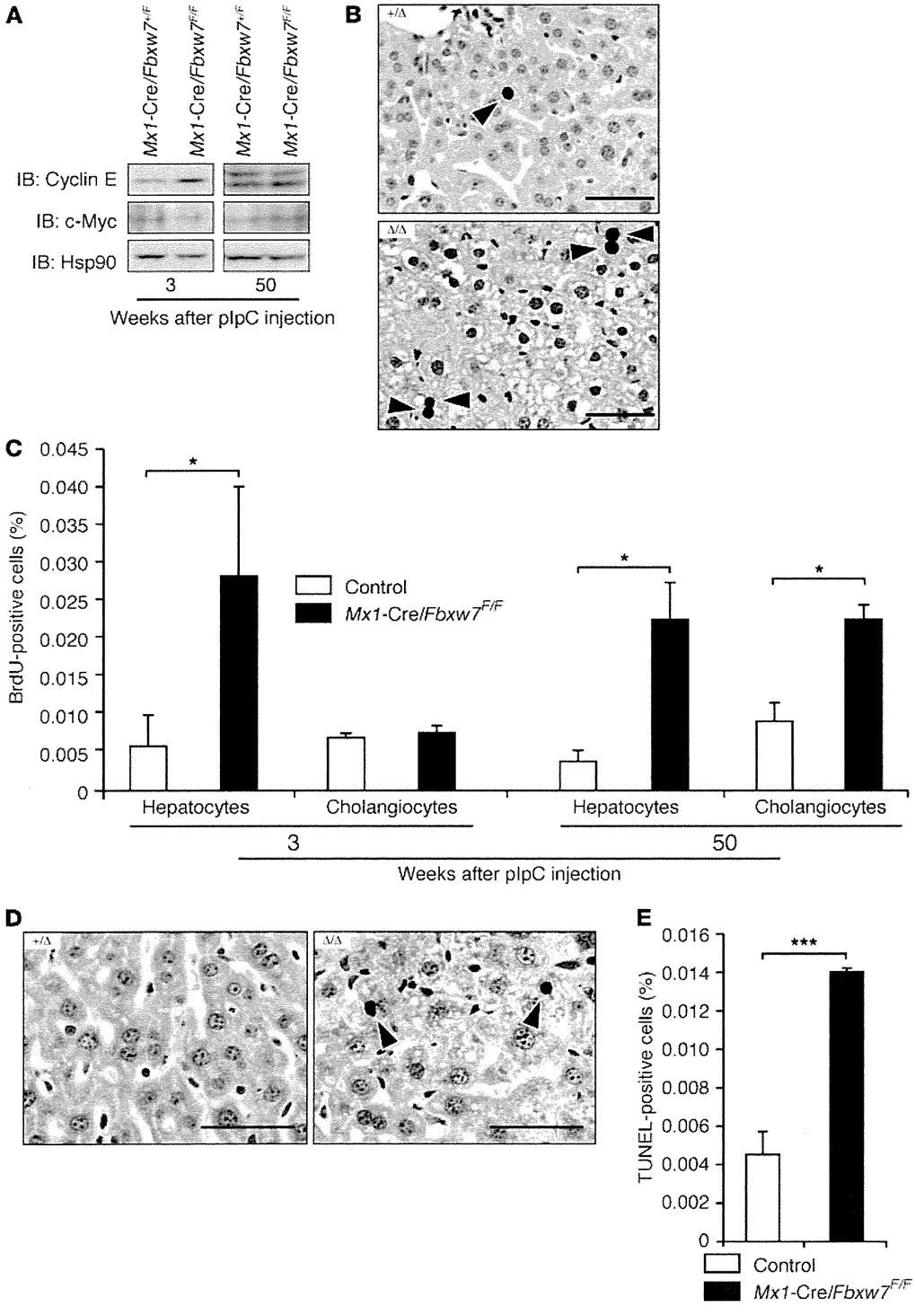

Figure 4
Increased proliferation and apoptosis of Fbxw7-deficient hepatocytes. (**A**) IB analysis of cyclin E, c-Myc, and Hsp90 (loading control) in liver extracts from *Mx1*-Cre/*Fbxw7*$^{+/F}$ and *Mx1*-Cre/*Fbxw7*$^{F/F}$ mice at 3 or 50 weeks after *Fbxw7* deletion by pIpC injection, beginning at 8 weeks of age. (**B**) Representative immunostaining for BrdU in liver sections from *Mx1*-Cre/*Fbxw7*$^{+/F}$ (+/Δ) and *Mx1*-Cre/*Fbxw7*$^{F/F}$ (Δ/Δ) mice injected with BrdU on 3 consecutive days, beginning 3 weeks after the final pIpC injection as in **A**. Arrowheads indicate BrdU-positive nuclei. Scale bar: 50 μm. (**C**) The proportion of BrdU-positive hepatocytes or cholangiocytes was determined from immunostaining for BrdU in combination with that for albumin or CK19 in the livers of *Mx1*-Cre/*Fbxw7*$^{+/F}$ (control) or *Mx1*-Cre/*Fbxw7*$^{F/F}$ mice at 3 or 50 weeks after deletion of *Fbxw7* as in **A**. Data are mean ± SD from 10 fields from 3 mice of each genotype. *$P < 0.05$. (**D**) Representative TUNEL staining for liver sections of *Mx1*-Cre/*Fbxw7*$^{+/F}$ (+/Δ) and *Mx1*-Cre/*Fbxw7*$^{F/F}$ (Δ/Δ) mice 3 weeks after the final pIpC injection as in **A**. Arrowheads indicate TUNEL-positive cells. Scale bar: 50 μm. (**E**) The proportion of TUNEL-positive liver cells was determined from images similar to those in **D**. Data are mean ± SD from 3 animals of each genotype. ***$P < 0.005$.

increase in the abundance of any of the isoforms of Notch in the liver of *Mx1*-Cre/*Fbxw7*$^{F/F}$ mice at either 3 or 50 weeks after *Fbxw7* deletion (data not shown), confocal microscopic analysis revealed that the intracellular domain of Notch1 was highly concentrated in both the cytoplasm and the nucleus of Fbxw7-deficient liver at 3 weeks after pIpC injection (Figure 6A). Consistent with the observed upregulation of Notch1, the abundance of Notch1 target genes, including those for Hes1 and Hey1, was simultaneously increased in the livers of *Mx1*-Cre/*Fbxw7*$^{F/F}$ mice (Figure 6B and Supplemental Figure 5A, respectively). At 15 weeks after pIpC injection, Notch1 accumulated in the hepatocyte-like cells residing around the portal area, and these cells were reactive to antibodies to CK7 (Figure 6C), another marker of cholangiocytes, suggesting that such cells might be in the process of transdifferentiation to the cholangiocytes by Notch activation. At 50 weeks after pIpC injection, Notch1 was observed in the form of aggregates in the

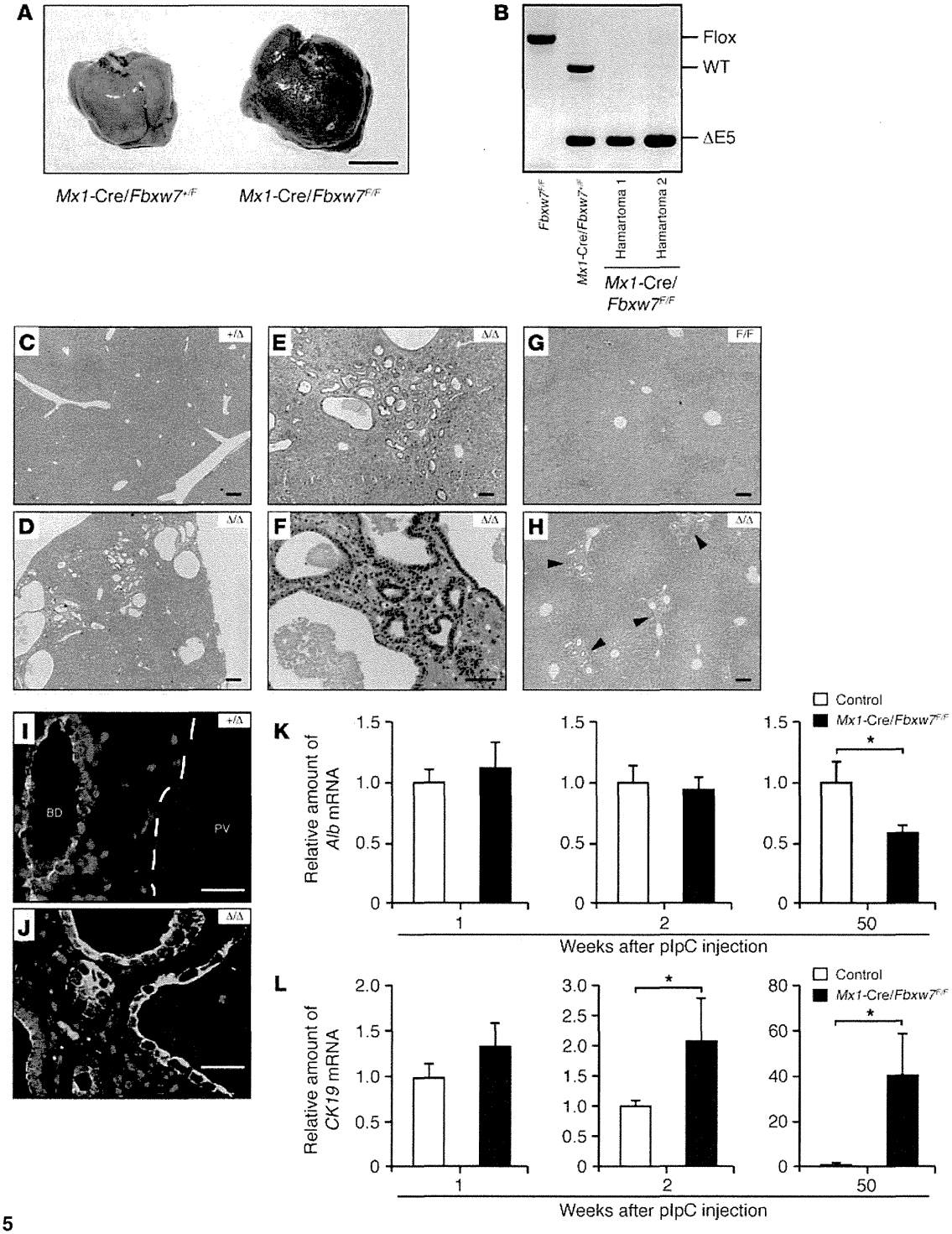

Figure 5

Hamartoma development as a result of long-term ablation of Fbxw7 in the liver. (**A**) Gross appearance of the livers of *Mx1*-Cre/*Fbxw7*$^{+/F}$ and *Mx1*-Cre/*Fbxw7*$^{F/F}$ mice at 50 weeks after the final injection of pIpC, beginning at 8 weeks of age. Scale bar: 10 mm. (**B**) PCR analysis of genomic DNA from the dilated bile ducts excised from hamartomas in the livers of 2 *Mx1*-Cre/*Fbxw7*$^{F/F}$ mice. Genomic DNA from control mice was also analyzed. (**C**–**F**) H&E staining of liver sections from a *Mx1*-Cre/*Fbxw7*$^{+/F}$ (+/Δ) mouse (**C**) and from a *Mx1*-Cre/*Fbxw7*$^{F/F}$ (Δ/Δ) mouse (**D**–**F**) that developed hamartoma after *Fbxw7* deletion as in **A**. (**G** and **H**) H&E staining of liver sections from *Fbxw7*$^{F/F}$ (F/F) and *Alb*-Cre/*Fbxw7*$^{F/F}$ (Δ/Δ) mice, respectively, at 12 weeks of age. Arrowheads indicate malformation of the ductal plate. Scale bar: 50 μm (**F**); 100 μm (**E**, **G**, and **H**); 200 μm (**C** and **D**). (**I** and **J**) Immunofluorescence staining for CK19 in the livers of *Mx1*-Cre/*Fbxw7*$^{+/F}$ (+/Δ) and *Mx1*-Cre/*Fbxw7*$^{F/F}$ (Δ/Δ) mice at 50 weeks after the final injection of pIpC, beginning at 8 weeks of age. The dashed line indicates the outer boundary of portal vein. PV, portal vein; BD, bile duct. Scale bar: 25 μm. (**K** and **L**) RT and real-time PCR analysis of *Alb* and *CK19* mRNAs, respectively, in the livers of *Mx1*-Cre/*Fbxw7*$^{+/F}$ (control) and *Mx1*-Cre/*Fbxw7*$^{F/F}$ mice at 1, 2, or 50 weeks after deletion of *Fbxw7* as in **A**. Normalized data are expressed relative to the corresponding value for control mice. Data are mean ± SD from 3 independent experiments. *$P < 0.05$.

cytoplasm or the nucleus (Supplemental Figure 4A). The increase in Hes1 or Hey1 was not detected by immunostaining analysis at this period (Supplemental Figure 4B and Supplemental Figure 5B), but the abundance of mRNAs for *Hes1*, *Hey1*, and *Hey2* was increased in the livers of *Mx1*-Cre/*Fbxw7*$^{F/F}$ mice at 50 weeks after pIpC injection (Figure 6D). Neither Notch2, mutations in the gene in which mutations result in Alagille disease, nor Notch3 or Notch4, the expression of both of which is increased in hepatocellular carcinoma, were detected by immunofluorescence analysis in the livers of either control or *Mx1*-Cre/*Fbxw7*$^{F/F}$ mice (data not shown). However, neither the expression of Notch ligands, such as Dll-1 and Jagged-1, nor that of the Notch cofactor RBP-J in the liver appeared to be affected by the loss of Fbxw7 (Supplemental Figure 6). We also examined the expression of TSC1 and TSC2, given that the loss of function of either TSC1 or TSC2 is known to result in the development of hamartoma in humans. However, no difference in expression of TSC1 or TSC2 was found between Fbxw7-deficient and control mice (Supplemental Figure 6).

To investigate whether the skewed developmental orientation toward the cholangiocyte lineage apparent in the Fbxw7-deficient liver is dependent on Notch1 accumulation, we examined the differentiation of hepatic stem cells in culture (45). A fraction containing hepatic stem cells was prepared from the livers of *Fbxw7*$^{+/F}$ and *Fbxw7*$^{F/F}$ embryos and was then infected with a retrovirus encoding Cre recombinase or with the empty virus alone to generate *Fbxw7*$^{+/F}$, *Fbxw7*$^{+/\Delta}$, *Fbxw7*$^{F/F}$, and *Fbxw7*$^{\Delta/\Delta}$ cells in the presence of HGF and EGF. Immunofluorescence analysis revealed that most of the *Fbxw7*$^{+/F}$, *Fbxw7*$^{+/\Delta}$, and *Fbxw7*$^{F/F}$ cells differentiated into the hepatocyte lineage, characterized by albumin expression, with only a small subset of cells differentiating into the cholangiocyte lineage (Figure 7A). In contrast, the percentage of *Fbxw7*$^{\Delta/\Delta}$ cells that differentiated into the cholangiocyte lineage, characterized by expression of CK7, was markedly increased compared with that for cells of the control genotypes. To confirm these results in a quantitative manner, we performed RT and real-time PCR analysis of *Alb* and *CK19* mRNAs. Consistent with the immunofluorescence data, the amount of *CK19* mRNA was significantly increased in *Fbxw7*$^{\Delta/\Delta}$ cells compared with that in *Fbxw7*$^{+/\Delta}$ cells, whereas the abundance of *Alb* mRNA did not differ between the 2 genotypes (Figure 7B).

Notch signaling is implicated in the differentiation of liver stem cells into the cholangiocyte lineage. Indeed, immunofluorescence analysis revealed that Notch1 accumulated in *Fbxw7*$^{\Delta/\Delta}$ cells to a greater extent than in *Fbxw7*$^{+/\Delta}$ cells (Supplemental Figure 7). We therefore examined whether additional ablation of the Notch cofactor RBP-J might correct the abnormal development of Fbxw7-deficient liver stem cells. We generated Fbxw7-deficient hepatic stem cells with additional deletion of either *Rbpj* or *Myc* genes and examined the level of *CK19* mRNA. The abundance of *CK19* mRNA was increased in *Fbxw7*$^{\Delta/\Delta}$*Myc*$^{\Delta/\Delta}$ cells but not in *Fbxw7*$^{\Delta/\Delta}$*Rbpj*$^{\Delta/\Delta}$ cells (Figure 7B). These results indicate that the skewed developmental orientation of hepatic stem cells to the cholangiocyte lineage is dependent on Notch1 accumulation induced by the loss of Fbxw7.

Discussion

Given that the substrates of Fbxw7 include key proteins that contribute to diverse biological processes, including the cell cycle, cell differentiation, and apoptosis, and that the binding of Fbxw7 to its substrates depends on their phosphorylation, the function of this protein is likely complex. Although much attention has focused on the relation between the accumulation of cyclin E due to loss of Fbxw7 function and tumorigenesis, Notch degradation by Fbxw7 is critical during embryogenesis, suggesting that Fbxw7 functions in development- and tissue-dependent manners. To provide insight into the physiological and pathological relevance of Fbxw7, we have induced conditional inactivation of *Fbxw7* in several mouse tissues. Our previous studies have shown that ablation of *Fbxw7* in hematopoietic cells or fibroblasts results in abnormalities that are mainly related to the cell cycle and apoptosis. We now show that liver-specific ablation of *Fbxw7* induced fatty liver and abnormal cell differentiation, likely as a result of the accumulation of SREBPs and Notch1, respectively, as well as promoted cell proliferation (Figure 8).

We generated 2 types of mice with liver-specific deficiency of Fbxw7 with the use of the *Mx1* or *Alb* gene promoters to drive Cre expression. The phenotypes of *Alb*-Cre/*Fbxw7*$^{F/F}$ mice are milder than those induced by acute ablation of Fbxw7 in *Mx1*-Cre/*Fbxw7*$^{F/F}$ mice, probably because of the operation of compensatory mechanisms during development in the former animals. In *Mx1*-Cre/*Fbxw7*$^{F/F}$ mice, it would be expected for *Fbxw7* to be deleted in cells and tissues other than the liver, such as hematopoietic cells. To exclude the possibility that ablation of Fbxw7 in hematopoietic cell lineages might be responsible for steatohepatitis, we have generated Lck-Cre/*Fbxw7*$^{F/F}$ and CD4-Cre/*Fbxw7*$^{F/F}$ mice (in both of which *Fbxw7* deletion occurs in T cells), CD19-Cre/*Fbxw7*$^{F/F}$ mice (*Fbxw7* deletion occurs in B cells), and LysM-Cre/*Fbxw7*$^{F/F}$ mice (*Fbxw7* deletion occurs in myeloid cells). None of these animals showed either fatty liver or hepatic inflammation (data not shown). Furthermore, *Alb*-Cre/*Fbxw7*$^{F/F}$ mice manifested pronounced hepatic infiltration of inflammatory cells when they were fed an MCD diet, confirming that the steatohepatitis induced by *Fbxw7* deletion is attributable to an effect that is intrinsic to the liver.

Nonalcoholic fatty liver disease (NAFLD) is a growing health concern, due to its rapidly increasing prevalence worldwide. NASH is a progressive form of NAFLD that has the potential to develop into hepatocellular carcinoma. We now show that mice with liver-specific ablation of Fbxw7 developed clinicopathologic features similar to those of NAFLD or NASH in humans, including triglyceride deposition around central veins, pericellular fibrosis, infiltration of inflammatory mononuclear cells, and the appearance of Mallory bodies in the liver as well as increases in the serum levels of ALT and AST. However, these animals were not found to develop hepatocellular carcinoma. Genetic mouse models for human NASH have been established by functional deletion of leptin (46) or its receptor (47), phosphatase and tensin homolog (PTEN) (48), NEMO (also known as IKK-γ) (49), interleukin-1 receptor α (50), galectin-3 (51), or retinoic acid receptor α (52). Mice transgenic for SREBP1c also manifest pronounced NASH (53). SREBP1c is degraded in an Fbxw7-dependent manner (16), and we have now shown that it accumulated in the Fbxw7-deficient liver. These findings thus suggest that an Fbxw7-SREBP1 axis plays a key physiological role in the regulation of lipid metabolism in the liver as well as a pathological role in the development of NASH.

Whereas steatosis develops in the acute phase of liver-specific Fbxw7 deficiency, hamartoma develops in the chronic phase. Fbxw7 targets mTOR for degradation (19). The TSC complex, consisting of TSC1 (hamartin) and TSC2 (tuberin), is the major negative regulator of mTOR, and its genetic loss results in mTOR

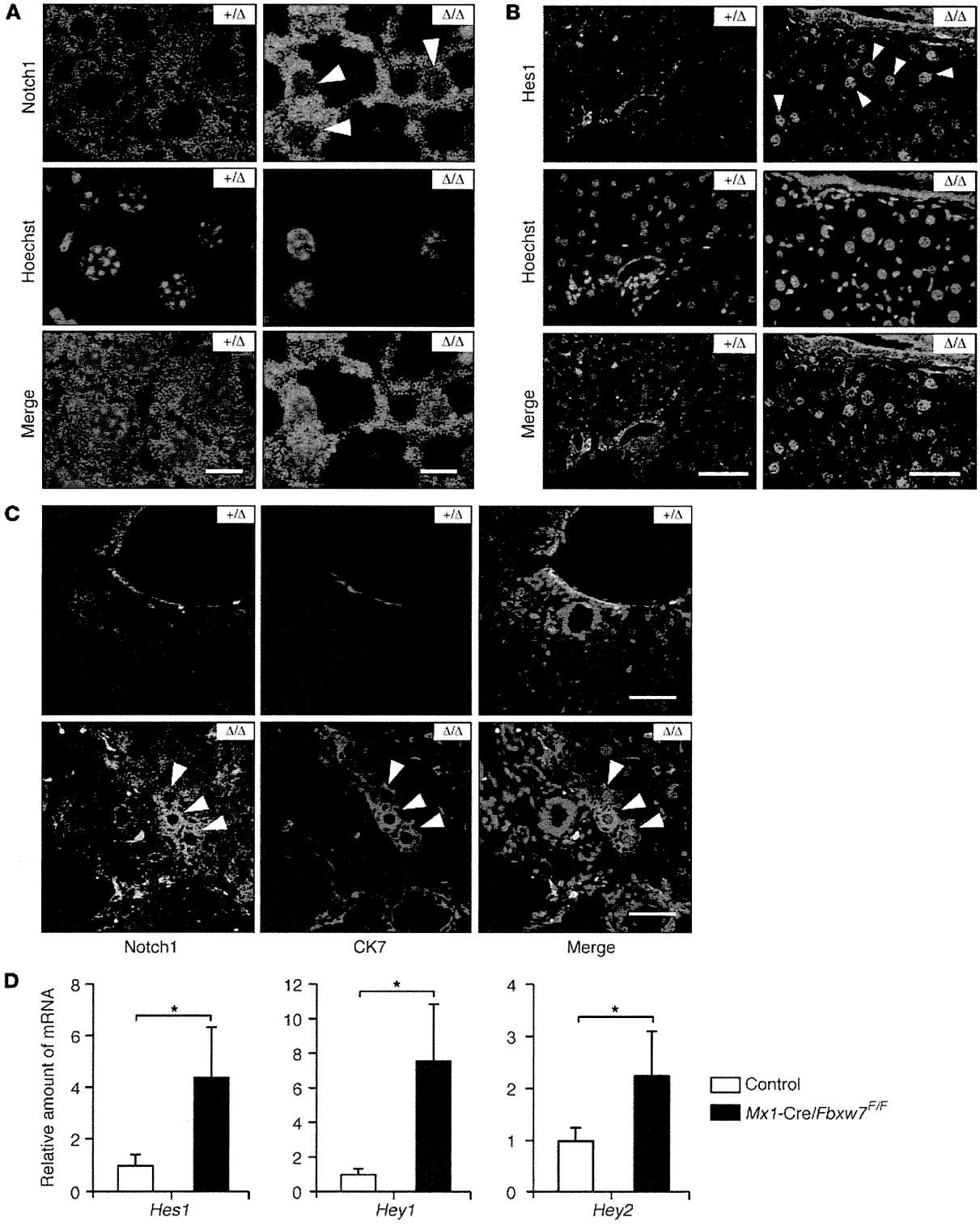

Figure 6

Accumulation of Notch1 and activation of its target genes in the Fbxw7-deficient liver. (**A** and **B**) Representative immunostaining for the intracellular domain of (**A**) Notch1 and for (**B**) Hes1 in liver sections from *Mx1*-Cre/*Fbxw7*$^{+/F}$ (+/Δ) and *Mx1*-Cre/*Fbxw7*$^{F/F}$ (Δ/Δ) mice at 3 weeks after *Fbxw7* deletion by pIpC injection, beginning at 8 weeks of age. Arrowheads indicate accumulating (**A**) Notch1 intracellular domain and (**B**) Hes1 in the nucleus. (**C**) Immunofluorescence staining for the intracellular domain of Notch1 and for CK7 in the livers of *Mx1*-Cre/*Fbxw7*$^{+/F}$ (+/Δ) and *Mx1*-Cre/*Fbxw7*$^{F/F}$ (Δ/Δ) mice at 15 weeks after the final injection of pIpC, beginning at 8 weeks of age. Intense Notch1 staining was detected in the Fbxw7-deficient liver, and most of the Notch1-positive cells express CK7 (arrowheads). Scale bar: 10 μm (**A**); 50 μm (**B** and **C**). (**D**) RT and real-time PCR analysis of Notch target genes in the livers of *Mx1*-Cre/*Fbxw7*$^{+/F}$ (control) and *Mx1*-Cre/*Fbxw7*$^{F/F}$ mice at 50 weeks after *Fbxw7* deletion. Normalized data for *Hes1*, *Hey1*, and *Hey2* mRNAs are expressed relative to the corresponding value for control mice and are mean ± SD from 3 independent experiments. *$P < 0.05$.

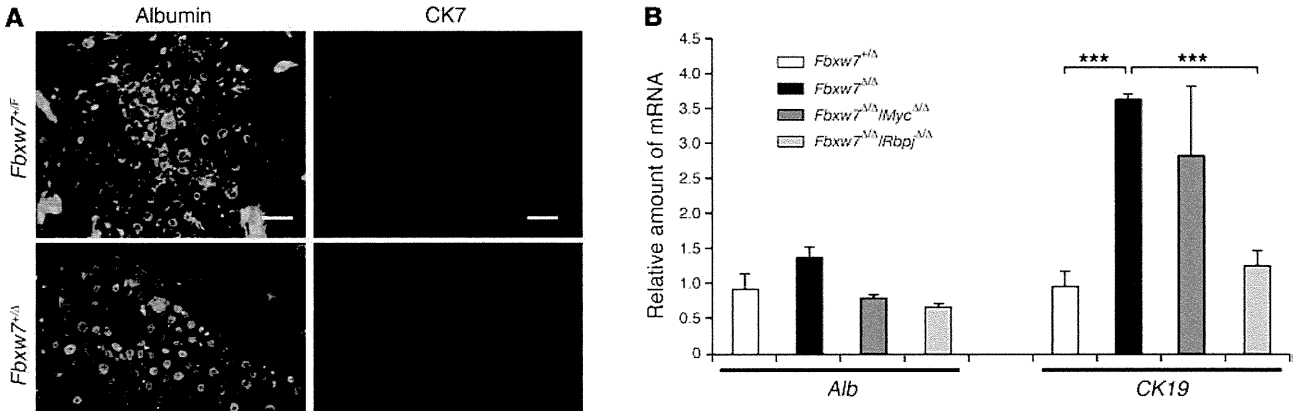

Figure 7
Skewed differentiation of hepatic stem cells from Fbxw7-deficient mice. (**A**) Primary cultured liver cells of the indicated genotypes were subjected to immunofluorescence staining with antibodies to albumin or to CK7. Clusters of cells expressing CK7 were apparent only with *Fbxw7*$^{\Delta/\Delta}$ cells. Scale bar: 50 μm. (**B**) RT and real-time PCR analysis of *Alb* and *CK19* mRNAs in primary cultured liver cells of the indicated genotypes. Normalized data for *Alb* and *CK19* mRNAs are expressed relative to the corresponding value for *Fbxw7*$^{+/\Delta}$ cells. Data are mean ± SD from 3 independent experiments. ***$P < 0.005$.

activation and development of hamartoma in humans (54, 55). However, the abundance of mTOR or TSC1/2 was not altered in the Fbxw7-deficient livers of mice, suggesting that the accumulation of mTOR or the loss of TSC1/2 is not responsible for hamartoma development in these animals. Microscopic examination revealed over proliferation of the biliary system in the hamartomas, suggesting that deregulated differentiation of liver stem cells into the cholangiocyte lineage might be largely responsible for hamartoma development. Liver stem cells are able to differentiate into either the hepatocyte or cholangiocyte lineages, with the Notch signaling pathway having been implicated in regulation of the cell fate decision by skewing differentiation toward the cholangiocyte lineage (41). We have now shown that both Notch1 and its target genes were overexpressed in the Fbxw7-deficient livers of mice and that the abnormal cell differentiation induced by Fbxw7 loss was corrected by the additional loss of the Notch cofactor RBP-J. These results suggest that Notch1 accumulation as a result of Fbxw7 loss is primarily responsible for the abnormal cell differentiation in the Fbxw7-deficient mouse liver. Although the origin of hamartomas as well as the mechanism of their development in the Fbxw7-deficient liver are currently unclear, transient activation of Notch proteins as a result of Fbxw7 loss may lead to a shift in cell differentiation from hepatocytes to cholangiocytes, and the generation of such abnormally differentiated cells might confer a predisposition to hamartoma development that is realized if the cells undergo an additional gene mutation. Mice lacking both Foxa1 and Foxa2 were recently shown to display a similar liver phenotype (hyperplasia of the biliary tree) (56). However, neither differentiation of hepatocytes nor Notch signaling were affected in Foxa1/2-deficient mice, whereas hyperactivation of Notch signaling seems to be attributable to the bile duct hamartoma in Fbxw7-deficient mice. Furthermore, proliferation of relatively small and uniform bile ducts is prominent in Foxa1/2-deficient mice, whereas the abnormal bile ducts in Fbxw7-deficient mice are large and heterogeneous in size. We therefore concluded that the mechanism underlying the development of proliferative bile ducts is likely different between these mutant mice.

Although Fbxw7 had been thought to function primarily in cell cycle control by regulating cyclin E, c-Myc, Notch, and c-Jun, the recent identification of additional substrates has suggested new cell cycle–independent roles for Fbxw7. We now provide genetic evidence that the major substrates of Fbxw7 in the liver are SREBP1 and Notch1, which accumulate in the Fbxw7-deficient liver and are responsible for liver steatosis and hamartoma development, respectively. These results contrast with our previous observations that deletion of *Fbxw7* in the hematopoietic system and fibroblasts results primarily in deregulation of the cell cycle or of apoptosis due to activation of the p53-dependent checkpoint (34–36). Why does the function of Fbxw7 differ in different tissues? We propose that the biological relevance of Fbxw7 is determined by 3 factors: (a) the expression of Fbxw7; (b) the expression and activation of protein kinases that phosphorylate the Cdc4 phosphodegron, an amino acid sequence that is recognized by Fbxw7; and (c) the expression of substrate molecules. The combination of these 3 factors may define the role of Fbxw7 in a tissue-specific manner, with the different phenotypes associated with Fbxw7 deficiency

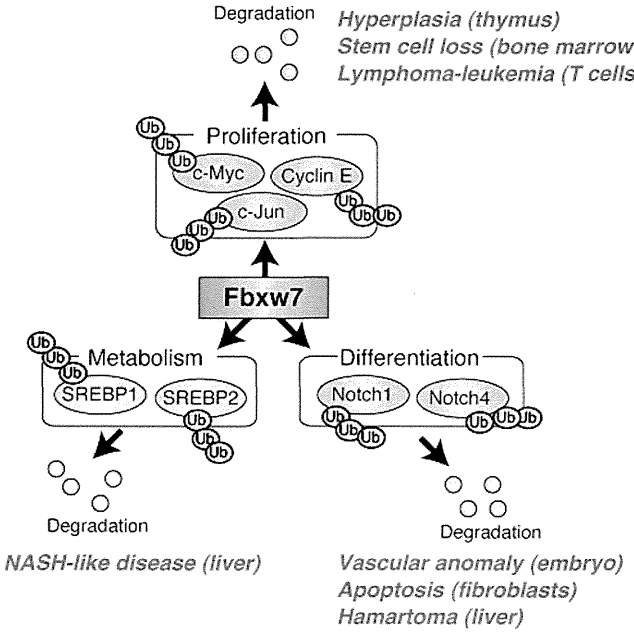

Figure 8
A model for Fbxw7 functions in vivo. Fbxw7 mediates ubiquitin-dependent degradation of substrates in different functional categories. For example, Fbxw7 controls cell proliferation by targeting c-Myc, cyclin E, and c-Jun for degradation. However, it also regulates lipid metabolism and cell differentiation by targeting SREBP and Notch proteins, respectively. Major phenotypes associated with Fbxw7 deficiency in different tissues are shown in red. Ub, ubiquitin.

being attributable to different expression patterns of Fbxw7, its substrates, and kinases that phosphorylate each substrate.

Methods

Generation of conditional knockout mice. Mice homozygous for the floxed *Fbxw7* allele (*Fbxw7*$^{F/F}$ mice) (34) were crossed with *Mx1*-Cre transgenic mice (57) provided by K. Rajewsky (Harvard Medical School, Boston, Massachusetts, USA) or *Alb*-Cre transgenic mice (58) purchased from The Jackson Laboratory. Expression of Cre recombinase in the resulting offspring of the former cross was induced by i.p. injection of 500 μg pIpC (GE Healthcare Biosciences) on 3 alternate days. Deletion of exon 5 of the floxed *Fbxw7* allele was confirmed by PCR analysis of genomic DNA as previously described (34). *Fbxw7*$^{F/F}$ mice were also crossed with *Rbpj*$^{F/F}$ mice (59) provided by T. Honjo (Kyoto University, Kyoto, Japan) or *Myc*$^{F/F}$ mice (60) provided by I.M. de Alborán (National Center for Biotechnology, Madrid, Spain). The experimental protocols were approved by the Institutional Animal Care and Use Committee of Kyushu University.

Histological and biochemical analysis. Liver tissue was fixed with 4% paraformaldehyde in PBS, embedded in paraffin, and stained with H&E or Masson's trichrome solution. Some sections were stained with Oil red O (Nakalai Tesque) according to standard procedures, in order to examine the extent of lipid accumulation in hepatocytes. Serum levels of AST and ALT were measured with a standard clinical autoanalyzer.

Dietary model of NASH. Mice were fed with an MCD diet (Funabashi Farm) for the indicated periods (see the legend for Figure 2) and analyzed.

Measurement of triglyceride and total cholesterol levels in the liver. Frozen liver tissue was homogenized, and triglyceride and total cholesterol were extracted from the homogenate with chloroform/methanol (2:1, vol/vol), dried, and resuspended in 2-propanol. The amounts of triglyceride and total cholesterol in the extract were measured with the use of Lipidos liquid and Cholescolor liquid kits (Toyobo), respectively.

Immunoblot analysis. Total protein extracts were prepared from liver with RIPA buffer. The extracts (30 μg) were subjected to immunoblot analysis as described previously (61) with antibodies to cyclin E (M-20), to c-Myc (N-262), to ChREBP (P-13), or to PPAR-γ (E-8), all of which were obtained from Santa Cruz Biotechnology Inc.; with antibodies to Ser^{2448}-phosphorylated or total (7C10) forms of mTOR (Cell Signaling Technology); with antibodies to SREBP1 (2A4, NeoMarkers); or with antibodies to PGC-1α (Chemicon). As a control, each membrane was stripped and then probed with antibodies to Hsp90 (BD Transduction Laboratories).

RT and real-time PCR analysis. Total RNA was extracted from liver using the guanidinium thiocyanate–phenol-chloroform method, purified, and subjected (1 μg) to RT with random hexanucleotide primers (ReverTra Ace α, Toyobo). The resulting cDNA was subjected to real-time PCR in a reaction mixture that contained 1× SYBR Green PCR Master Mix (Applied Biosystems) and 200 nM of gene-specific primers. Assays were performed in triplicate with an ABI Prism 7700 Sequence Detector (Applied Biosystems). The PCR protocol comprised 40 cycles of incubation at 60°C for 30 seconds and 95°C for 5 seconds. The sequences of the PCR primers (sense and antisense, respectively) were 5′-TGCTCCCAGCTGCAGGC-3′ and 5′-GCCCGGTAGCTCTGGGTGTA-3′ for *Fas*, 5′-TGGGTTGGCTGCTTGTG-3′ and 5′-GCGTGGGCAGGATGAAG-3′ for *Scd1*, 5′-CTGCCGACCTGATGAATTCC-3′ and 5′-TAGGGCCATCACACTGTGTC-3′ for *Ldlr*, 5′-GCTCTCCATACAGTGCTACC-3′ and 5′-GAGTGAAAGATCATGAAGCC-3′ for *Hmgcs1*, 5′-AGAGATGCCATCTCCAGCCTC-3′ and 5′-CTTGGTCTTAGGGTCTTCAGG-3′ for *ChREBP*, 5′-CTGTGAAGTTCAATGCACTGGAA-3′ and 5′-CCTCGATGGGCTTCACGTT-3′ for *Pparg*, 5′-CATGGATTGCACATTTGAAG-3′ and 5′-CCTGTGTCCCCTGTCTCA-3′ for *SREBP1c*, 5′-TCCTGTGCTGCAGCCTTTCTCA-3′ and 5′-CCAGGTTCCCACAAAGGCATCA-3′ for fatty acid–binding protein 4, 5′-GTCCTACAGATTGACAATGC-3′ and 5′-CACGCTCTGGATCTGTGACAG-3′ for *CK19*, 5′-CATGACACCATGCCTGCTGAT-3′ and 5′-CTCTGATCTTCAGGAAGTGTAC-3′ for *Alb*, 5′-CATTCCAAGCTAGAGAAGGCAG-3′ and 5′-TATTTCCCCAACACGCTCG-3′ for *Hes1*, 5′-AAAATGCTGCACACTGCAGG-3′ and 5′-CGAGTCCTTCAATGATGCTCAG-3′ for *Hey1*, 5′-AAACGACCTCCGAAAGCGA-3′ and 5′-CGGTGAATTGGACCTCATCACT-3′ for *Hey2*, and 5′-GGAACATAGCCGTAAACTGC-3′ and 5′-TCACTGTGCCTGAACTTACC-3′ for β-tubulin. Reactions for β-tubulin mRNA were performed concurrently on the same plate as those for the test mRNAs, and results were normalized by the corresponding amount of β-tubulin mRNA.

BrdU incorporation in vivo. Mice were injected with BrdU (1 mg, i.p.) on 3 consecutive days. The liver was removed 24 hours after the third injection of BrdU, and BrdU incorporation was examined with an In Situ BrdU Detection Kit (BD Biosciences). BrdU-positive cells were counted in 10 different fields at high (×400) magnification, and the percentage of BrdU-positive cells was calculated.

Immunofluorescence microscopy. Liver tissue was fixed with 4% paraformaldehyde in PBS and sectioned at a thickness of 40 μm with a vibratome. Sections were then immunostained with antibodies to the intracellular domain of Notch1 or to SCD-1 (both from Cell Signaling Technology), to Hes1 (AB5702, Millipore), to SREBP1 (2A4, NeoMarkers), to albumin (Biogenesis), to CK19 (45), or to CK7 (MAB3226, Chemicon). Immune complexes were detected with Alexa Fluor 488– or Alexa Fluor 546–conjugated goat antibodies to mouse or rabbit IgG (Invitrogen). Cultured liver cells were also subjected to immunostaining, as described previously (45), with the antibodies to albumin and to CK7. For confocal microscopic analysis, we used Zeiss LSM 510 META Confocal Microscope (Carl Zeiss MicroImaging).

TUNEL assay. The TUNEL assay was performed as described previously (62). In brief, paraffin-embedded sections of liver were treated with H_2O_2,

permeabilized for 15 minutes at 37°C with proteinase K (20 μg/ml, Sigma-Aldrich), and then incubated for 1 hour at 37°C with a reaction mixture containing terminal deoxynucleotidyl transferase (Invitrogen) and biotinylated dUTP (Boehringer Ingelheim). Labeled DNA was visualized with an ABC Kit (Vector Laboratories) and diaminobenzidine.

Primary culture of fetal hepatocytes. For the preparation of a single-cell suspension, the livers of mice at E13.5 were dissociated in culture medium (DMEM supplemented with 10% FBS, γ-insulin [1 μg/ml, Wako], 0.1 μM dexamethasone [Sigma-Aldrich], 10 mM nicotinamide [Sigma-Aldrich], 2 mM L-glutamine [Gibco BRL], 50 μM β-mercaptoethanol [Sigma-Aldrich], 5 mM HEPES [Wako], and penicillin-streptomycin [Gibco BRL]) by repeated passage of the tissue through the mouth of a pipette. Human recombinant HGF (50 ng/ml, Sigma-Aldrich) and EGF (20 ng/ml, Sigma-Aldrich) were added to the cells at 24 hours after culture initiation. Cells were seeded at a density of 1×10^6 cells per well in 6-well plates for infection with retroviruses as described below (45).

Gene deletion in cultured cells by retroviral infection. cDNA encoding Cre recombinase was subcloned into the retroviral vector pMX-puro provided by T. Kitamura (University of Tokyo, Tokyo, Japan), and the resulting construct was introduced into Plat E packaging cells (63) with the use of the FuGENE6 reagent (Roche). The resulting culture supernatants containing the recombinant ecotropic retrovirus were harvested and incubated for 24 hours in the presence of Polybrene (2 μg/ml; Sigma-Aldrich) with proliferating liver cells harboring floxed alleles of *Fbxw7*, *Rbpj*, or *Myc*. The cells were cultured for an additional 24 hours in virus-free medium, subjected to selection in medium containing puromycin (3 μg/ml), cultured for 96 hours in puromycin-free medium, and then harvested.

Statistics. Data are presented as mean ± SD and were analyzed using 2-tailed Student's *t* test. A *P* value of less than 0.05 was considered statistically significant.

Acknowledgments

We thank T. Honjo for *Rbpj* floxed mice; I.M. de Alborán for *Myc* floxed mice; K. Rajewsky for *Mx1*-Cre transgenic mice; T. Kitamura for pMX-puro; S. Aishima, Y. Nishihara, M. Sakamoto, and R. Irie for discussion; N. Kitajima, Y. Yamada, and K. Takeda for technical assistance; members of our laboratories for comments on the manuscript; and A. Ohta and M. Kimura for help in the preparation of the manuscript. This work was supported in part by a grant from the Ministry of Education, Culture, Sports, Science, and Technology of Japan and by a research grant from the Takeda Science Foundation.

Received for publication August 6, 2009, and accepted in revised form September 29, 2010.

Address correspondence to: Keiichi I. Nakayama, Department of Molecular and Cellular Biology, Medical Institute of Bioregulation, Kyushu University, 3-1-1 Maidashi, Higashi-ku, Fukuoka, Fukuoka 812-8582, Japan. Phone: 81.92.642.6815; Fax: 81.92.642.6819; E-mail: nakayak1@bioreg.kyushu-u.ac.jp.

1. Hershko A, Ciechanover A. The ubiquitin system. *Annu Rev Biochem.* 1998;67:425–479.
2. Nakayama KI, Nakayama K. Ubiquitin ligases: cell-cycle control and cancer. *Nat Rev Cancer.* 2006; 6(5):369–381.
3. Frescas D, Pagano M. Deregulated proteolysis by the F-box proteins SKP2 and beta-TrCP: tipping the scales of cancer. *Nat Rev Cancer.* 2008;8(6):438–449.
4. Welcker M, Clurman BE. FBW7 ubiquitin ligase: a tumour suppressor at the crossroads of cell division, groWTh and differentiation. *Nat Rev Cancer.* 2008;8(2):83–93.
5. Hubbard EJ, Wu G, Kitajewski J, Greenwald I. *sel-10*, a negative regulator of *lin-12* activity in *Caenorhabditis elegans*, encodes a member of the CDC4 family of proteins. *Genes Dev.* 1997;11(23):3182–3193.
6. Sundaram M, Greenwald I. Suppressors of a *lin-12* hypomorph define genes that interact with both *lin-12* and *glp-1* in *Caenorhabditis elegans*. *Genetics.* 1993;135(3):765–783.
7. Gupta-Rossi N, et al. Functional interaction between SEL-10, an F-box protein, and the nuclear form of activated Notch1 receptor. *J Biol Chem.* 2001;276(37):34371–34378.
8. Oberg C, Li J, Pauley A, Wolf E, Gurney M, Lendahl U. The Notch intracellular domain is ubiquitinated and negatively regulated by the mammalian Sel-10 homolog. *J Biol Chem.* 2001;276(38):35847–35853.
9. Koepp DM, et al. Phosphorylation-dependent ubiquitination of cyclin E by the SCF^{Fbw7} ubiquitin ligase. *Science.* 2001;294(5540):173–177.
10. Moberg KH, Bell DW, Wahrer DC, Haber DA, Hariharan IK. Archipelago regulates Cyclin E levels in Drosophila and is mutated in human cancer cell lines. *Nature.* 2001;413(6853):311–316.
11. Strohmaier H, Spruck CH, Kaiser P, Won KA, Sangfelt O, Reed SI. Human F-box protein hCdc4 targets cyclin E for proteolysis and is mutated in a breast cancer cell line. *Nature.* 2001;413(6853):316–322.
12. Yada M, et al. Phosphorylation-dependent degradation of c-Myc is mediated by the F-box protein Fbw7. *EMBO J.* 2004;23(10):2116–2125.
13. Welcker M, et al. The Fbw7 tumor suppressor regulates glycogen synthase kinase 3 phosphorylation-dependent c-Myc protein degradation. *Proc Natl Acad Sci U S A.* 2004;101(24):9085–9090.
14. Nateri AS, Riera-Sans L, Da Costa C, Behrens A. The ubiquitin ligase SCF^{Fbw7} antagonizes apoptotic JNK signaling. *Science.* 2004;303(5662):1374–1378.
15. Wei W, Jin J, Schlisio S, Harper JW, Kaelin WG Jr. The v-Jun point mutation allows c-Jun to escape GSK3-dependent recognition and destruction by the Fbw7 ubiquitin ligase. *Cancer Cell.* 2005;8(1):25–33.
16. Sundqvist A, et al. Control of lipid metabolism by phosphorylation-dependent degradation of the SREBP family of transcription factors by SCF^{Fbw7}. *Cell Metab.* 2005;1(6):379–391.
17. Punga T, Bengoechea-Alonso MT, Ericsson J. Phosphorylation and ubiquitination of the transcription factor sterol regulatory element-binding protein-1 in response to DNA binding. *J Biol Chem.* 2006;281(35):25278–25286.
18. Bengoechea-Alonso MT, Ericsson J. A phosphorylation cascade controls the degradation of active SREBP1. *J Biol Chem.* 2009;284(9):5885–5895.
19. Mao JH, et al. FBXW7 targets mTOR for degradation and cooperates with PTEN in tumor suppression. *Science.* 2008;321(5895):1499–1502.
20. Olson BL, et al. SCF^{Cdc4} acts antagonistically to the PGC-1alpha transcriptional coactivator by targeting it for ubiquitin-mediated proteolysis. *Genes Dev.* 2008;22(2):252–264.
21. Maser RS, et al. Chromosomally unstable mouse tumours have genomic alterations similar to diverse human cancers. *Nature.* 2007;447(7147):966–971.
22. Lee JW, et al. Mutational analysis of the hCDC4 gene in gastric carcinomas. *Eur J Cancer.* 2006; 42(14):2369–2373.
23. Kemp Z, et al. CDC4 mutations occur in a subset of colorectal cancers but are not predicted to cause loss of function and are not associated with chromosomal instability. *Cancer Res.* 2005; 65(24):11361–11366.
24. Hubalek MM, et al. Cyclin E dysregulation and chromosomal instability in endometrial cancer. *Oncogene.* 2004;23(23):4187–4192.
25. Koh MS, Ittmann M, Kadmon D, Thompson TC, Leach FS. CDC4 gene expression as potential biomarker for targeted therapy in prostate cancer. *Cancer Biol Ther.* 2006;5(1):78–83.
26. Calhoun ES, et al. BRAF and FBXW7 (CDC4, FBW7, AGO, SEL10) mutations in distinct subsets of pancreatic cancer: potential therapeutic targets. *Am J Pathol.* 2003;163(4):1255–1260.
27. Akhoondi S, et al. FBXW7/hCDC4 is a general tumor suppressor in human cancer. *Cancer Res.* 2007;67(19):9006–9012.
28. Song JH, Schnittke N, Zaat A, Walsh CS, Miller CW. FBXW7 mutation in adult T-cell and B-cell acute lymphocytic leukemias. *Leuk Res.* 2008; 32(11):1751–1755.
29. Thompson BJ, et al. The SCF^{FBW7} ubiquitin ligase complex as a tumor suppressor in T cell leukemia. *J Exp Med.* 2007;204(8):1825–1835.
30. O'Neil J, et al. FBW7 mutations in leukemic cells mediate NOTCH pathway activation and resistance to gamma-secretase inhibitors. *J Exp Med.* 2007;204(8):1813–1824.
31. Malyukova A, et al. The tumor suppressor gene hCDC4 is frequently mutated in human T-cell acute lymphoblastic leukemia with functional consequences for Notch signaling. *Cancer Res.* 2007;67(12):5611–5616.
32. Tsunematsu R, et al. Mouse Fbw7/Sel-10/Cdc4 is required for notch degradation during vascular development. *J Biol Chem.* 2004;279(10):9417–9423.
33. Tetzlaff MT, et al. Defective cardiovascular development and elevated cyclin E and Notch proteins in mice lacking the Fbw7 F-box protein. *Proc Natl Acad Sci U S A.* 2004;101(10):3338–3345.
34. Onoyama I, et al. Conditional inactivation of Fbxw7 impairs cell-cycle exit during T cell differentiation and results in lymphomatogenesis. *J Exp Med.* 2007;204(12):2875–2888.
35. Matsuoka S, et al. Fbxw7 acts as a critical fail-safe against premature loss of hematopoietic stem cells and development of T-ALL. *Genes Dev.* 2008;22(8):986–991.
36. Ishikawa Y, Onoyama I, Nakayama KI, Nakayama K. Notch-dependent cell cycle arrest and apoptosis in mouse embryonic fibroblasts lacking Fbxw7. *Oncogene.* 2008;27(47):6164–6174.
37. Matteoni CA, Younossi ZM, Gramlich T, Boparai N, Liu YC, McCullough AJ. Nonalcoholic fatty liver disease: a spectrum of clinical and pathological